NASA CONTRACTOR REPORT 166389

Aeroelastic Stability of Rotor Blades Using Finite Element Analysis

Inderjit Chopra and Nithiam Ti Sivaneri

NASA Cooperative Agreement NCC 2-13
August 1982

NASA

Page intentionally left blank

NASA CONTRACTOR REPORT 166389

Aeroelastic Stability of Rotor Blades Using Finite Element Analysis

Inderjit Chopra and Nithiam Ti Sivaneri
Joint Institute for Aeronautics and Astronautics
Stanford University, California

Prepared for Ames Research Center
under NASA Cooperative Agreement NCC 2-13

National Aeronautics and
Space Administration

Ames Research Center
Moffett Field, California 94035

TABLE OF CONTENTS

LIST OF TABLES

LIST OF FIGURES

ABSTRACT

The flutter stability of flap bending, lead-lag bending, and torsion of helicopter rotor blades in hover is investigated using a finite element formulation based on Hamilton's principle. The blade is divided into a number of finite elements. Quasi-steady strip theory is used to evaluate the aerodynamic leads. The nonlinear equations of motion are solved for steady-state blade deflections through an iterative procedure. The equations of motion are linearized assuming blade motion to be a small perturbation about the steady deflected shape. The normal-mode method based on the coupled rotating natural modes is used to reduce the number of equations in the flutter eigenanalysis. First the formulation is applied to single-load-path blades, for example, articulated and hingeless blades. Numerical results show very good agreement with existing results obtained using a modal approach. The second part of the application concerns multiple-load-path blades, namely bearingless blades. The flexure of a bearingless blade consists of multiple beams (flexbeams and torque tube) leading to redundancy. The formulation is modified so that the multibeams of the flexure could be modelled individually. Numerical results are presented for several analytical models of the bearingless blade. Results are also obtained using an equivalent beam appraoch (the common approach) wherein a bearingless blade is modelled as a single beam with equivalent properties. The comparison between the two sets of results show that the equivalent beam modelling is inaccurate.

NOMENCLATURE

a	lift-curve slope
A	blade cross-section area
B_1, B_2	blade cross-section integrals
c	blade chord
C_L	blade-section lift coefficient
$C_{M_{ac}}$	blade-section pitching moment coefficient
C_T	rotor thrust coefficient
C_1, C_2	blade cross-section integrals
e_a	tension-center offset from elastic axis, positive forward
e_d	aerodynamic-center offset from elastic axis, positive aft
e_g	center-of-mass offset from elastic axis, positive forward
E	Young's modulus
F	centrifugal force
GJ	blade elastic torsion stiffness
I_y, I_z	blade cross-section moments of inertia in the flap and lead-lag directions, respectively
k_A	polar radius of gyration of blade cross section, $\sqrt{(I_y + I_z)/A}$
k_m	mass radius of gyration of blade cross section, $\sqrt{(k_{m1}^2 + k_{m2}^2)}$
k_{m1}, k_{m2}	principal mass radii of gyration of blade cross section
l_i	length of ith element
L_u, L_v, L_w	aerodynamic forces per unit length in u, v, w directions, respectively
m	mass per unit length of blade
M_ϕ	aerodynamic moment per unit length about elastic axis

n	number of elements
$\{q\}$	vector of global degrees of freedom
R	rotor radius
t	time
u, v, w	elastic displacements in x, y, z directions, respectively
U_P, U_T	blade cross-section air velocity components in negative η and ς directions, respectively
v_i	induced inflow
V	blade cross-section resultant air velocity
x, y, z	undeformed blade coordinates
x_i	local axial coordinate of the ith element
α	blade cross-section angle of attack
β_p	blade precone angle
γ	Lock number, $3\rho acR/m$
$\delta T, \delta U$	variation of kinetic and strain energies, respectively
δW	virtual work done due to aerodynamic loads
θ	blade prepitch
λ_i	rotor inflow ratio, $v_i/\Omega R$
ξ, η, ς	deformed-blade coordinates
σ	solidity ratio
ϕ	elastic twist about elastic axis
$\hat{\phi}$	geometric twist about elastic axis
ψ	dimensionless time, Ωt
$\omega_v, \omega_w, \omega_\phi$	fundamental coupled rotating lead-lag, flap, torsion natural requencies, respectively

Ω	rotor blade angular velocity
$()'$	$\partial()/\partial x$
$\dot{()}$	$\partial()/\partial \psi$

1. INTRODUCTION

Helicopter dynamics is a complex problem involving nonlinear structural, inertial, and aerodynamic forces. For efficient blade designs, there is an increasing trend toward nonuniformity in structural and aerodynamic properties. The root geometry is complex.

Most of the helicopters in service employ either an articulated or a teetering rotor. In recent years, there has been considerable interest in alternate designs with an eye toward mechanical simplicity and increased maintainability. The hingeless and bearingless rotors are the outgrowth of such efforts. A conventional articulated rotor blade has mechanical flap and lag hinges, a lag damper and a pitch bearing. Figure 1 shows the schematic of an articulated blade hub and root. A hingeless blade, as the name implies, lacks the hinges and is cantilevered at the hub. It does have a pitch bearing for pitch control. A bearingless design eliminates the hinges and the pitch bearing as well. Only some hingeless and bearingless designs include lag dampers. The bearingless blade has an elastic flexure consisting of flexbeams and a torque tube to facilitate pitch changes. An example (Fig. 2) that has been tested in flight and wind dunnel is the Boeing- Vertol designed Bearingless Main Rotor, BMR [Dixon and Bishop (1980); and Warmbrodt and McCloud (1981)]. The BMR flexure (Fig. 3) extends from the hub to about 25%blade radius where it is connected to the outboard blade by a rigid clevis. The flexure consists of two parallel, torsionally-soft, open-section beams and a torsionally-stiff (flexurally-soft) torque tube. The inboard end of the torque tube is connected to a pitch link via a pitch horn at the hub; and the outboard end is attached to the clevis. The pitch control to the blade is applied through the torque tube by rotating the blade-root clevis which elastically twists the flexbeams. The blade outboard of clevis is of airfoil section and is similar to a conventional blade. The articulated and

hingeless blades are referred to as single-load-path blades and the bearingless blade as multiple-load-path blade. This is because the blade loads can be transmitted to the hub by redundant paths of the flexure in the case of a bearingless blade.

To help in the design of helicopter rotor blades, it is necessary to solve for trim deflections and to determine the aeroelastic stability in hover and forward flight. The aeroelastic stability of articulated blades is well understood. In the case of hingeless and bearingless blades, the absence of hinge motion modifies the dynamic characteristics of the blade and may significantly influence the aeroelastic stability. Not enough is known about the parameters affecting the aeroelastic behavior of bearingless blades. The influence of multilple load paths on aeroelastic stability is not fully understood.

The simplest form of roptor blade representation is the rigid blade model with spring restrained hinges [Ormiston and Hodges (1972) and Kaza and Kvaternik (1976)]. For this model, the trim solution is generally obtained from coupled linear or nonlinear flap-lag equations and the flutter stability is determined assuming linear perturbation motion about the trim solution. This type of modelling is satisfactory for simple blade configurations such as articulated. A more appropriate representation is to treat the rotor blade as an elastic beam. Houbolt and Brooks (1958) have derived the differential equations of motion for the combined bending and torsion of an elastic blade. Several authors [Hodges and Dowell (1974), Kvaternik and Kaza (1976), and Rosen and Friedmann (1978)] have modified these equations to consistently include nonlinear structural and inertial terms for moderately large deflections. A number of researchers have analysed the aeroelastic stability of hingeless blades with elastic-beam modelling. Examples are Hodges and Ormiston (1976) and Johnson (1977). The common approach for calculating the trim deflections, as well as the aeroelastic stability, is the modal method (for example, the Galerkin method) using coupled natural modes. In general, the trim deflections are assumed

to be large and obtained by solving nonlinear steady-state equations; and the flutter equations of motion are linearized about the trim state. This linearization simplifies the stability analysis. There have been some attempts at determining the stability using a complete nonlinear analysis such as the limit cycle analysis. These have been for simple blade models. For example, Friedmann and Tong (1973) consider a flap-lag blade; and the analysis of Chopra and Dugundji (1979) includes the torsion degree of freedom but the blade is modelled as rigid with spring restrained hinges.

The theoretical analysis of a bearingless blade is more involved than that of a hingeless blade primarily due to the redundancy of the flexure. Several authors have examined the aeroelastic stabililty of bearingless blades. Bielawa (1976) has given a theoretical analysis for composite bearingless rotor blades and experimental results from dynamically scaled models. The formulation is made for a blade with one flexbeam and a torque tube. Hodges (1979) has analyzed bearingless configurations with single flexbeam. The bending stiffness of the torque tube is neglected. The outboard blade is treated as rigid. Hodges has used an equivalent-beam approach to model the twinbeam root flexure of the BMR blade. Harvey (1976) has modelled a single-flexbeam bearingless blade by lumped massed connected by elastic beam elements. If any of the analyses mentiond above are used to study the BMR blade, then the twinbeams of the the flexure has to be modelled as single flexbeam with equivalent properties. The equivalent properties can be obtained by matching the fundamental frequencies of the equivalent-beam model with that of the multibeam blade.

With the modal approach, it becomes increasingly difficult to handle geometric coomplexities. For example, it is difficult to efectively model the multibeam flexure of a bearingless blade. The finite element method [Gallagher (1975)] has been extensively used in linear structural analysis. The structure is divided into a number of finite elements and the application of energy principles, or the method of weighted

residuals, yields approximate expressions for forces (inertial, elastic, etc.) over each element. The global equations of motion are obtained by assembling the elements. Nonuniform properties can be easily accommodated. The finite element method is very flexible and the formulation can be adapted to different rotor blade configurations with a few modifications. Multibeams of a bearingless blade can be modelled individually.

The finite element method has been applied for the determiniation of free-vibration characteristics of rotating one dimensional (flap bending) beams by many authors. A few examples are Nagaraj and Shanthakumar (1975), Putter and Manor (1978), and Hodges and Rutkowski (1981). It is common practice to use simple beam elements (represented by end nodes) satisfying the continuity of displacement and slope between elements. Refined elements with internal nodes may be used instead. One can attain a desired accuracy by using either simple or refined beam elements, but, if simple elements are used, a greater number of them may be necessary. However, the assembly of simple elements results in narrowly banded matrices; the assembled matrices for refined elemnts are more populated. Murty and Raman (1980) have used the finite element method for computing the nonlinear response of a rotating beam under prescribed forces.

Yasue (1978) has obtained the natural-vibration characteristics of a hingeless blade in combined flap bending, lag bending, and torsion using a finite element formulation. The normal mode method based on these natural modes is utilized to calculate the trim solution and the response of the blade under gust loading. Yasue's finite elements exhibit the interelement continuity of the torsional deflection as well as its slope; and hence a blade with jumps in torsional rigidity cannot be handled. Friedmann and Straub (1980) and Straub and Friedmann and Straub (1981) have applied a finite element formulation based on the method of weighted residuals to calculate the free-vibration characteristics of a flap-lag hingeless blade. Then, the

trim state, flutter stability, and response of the blade in hover and forward flight have been computed using a modal approach. These three rdeferences use the finite element method just to obtain the natural modes; the trim solution is based on a modal approach.

In the present research, a finite element formulation is developed to investigate the flutter stability of flap bending, lead-lag bending, and torsion of rotor blades in hover. The formulation is made for a nonuniform blade with pretwist and precone, and having chordwise offsets of the center of mass, aerodynamic center, and tension center from the elastic axis. The deflections considered are the axial, lead-lag, and flap deflections of the elastic axis and a torsional deflection about the elastic axis. The spatial dependence of the deflections is made discrete by dividing the blade into a number of elements. Approximate expressions for element forces are obtained applying Hamilton's principle; and the assembly of elements results in the global equations of motion in terms of the nodal degrees of freedom. The aerodynamic loads are based on quasi-steady strip theory. The trim solution is computed from nonlinear steady state equations without making a modal transformation. The coupled rotating natural-vibration characteristics are calculated about the trim condition. The flutter motion is assumed to be a small perturbation about the trim state. The normal mode method based on the rotating natural modes is used to solve the linearized flutter equations as an eigenvalue problem. Flutter stability is inferred by studying the flutter eigenvalues.

Here it should be pointed out that the emphasis of the present study is on the feasibility of the application of the finite-element method to rotor blade aeroelasticity; and hence, importance is not given to certain aerodynamic aspects such as compressibility effects and the effects of preceding and returning wakes. A brief review of the research in these areas follows. It is popular to use a quasisteady strip theory approximation without wake effects for estimating the unsteady loads

on a rotor, one of the main reasons being the difficulties involved in accuractely representing the Theodorsen function $c(\kappa)$. The difficulties arise because, unlike that of fixed wings, the wake of one rotor blade interacts with that of the others. The first significant attempts at unsteady aerodynamic theories for rotary wings in incompressible flow are due to Loewy (1957), Timman and Van De Vooren (1957), and Jones (1958). A theory to study the compressiblity effects including wake is presented by Jones and Rao (1970); aerodynamic coefficients for certain Mach numbers and frequencies are given in this paper. In another study, on the effects of tip vortices on rotor blades in hovering flight, Jones and Rao (1971) colclude that the use of two-dimensional strip theory would not result in serious error provided the blades oscillate at several cycles per rotation. Murthy and Pierce (1976) formulate a technique for the prediction of flutter of a helicopter rotor in hover and axial flight in such a manner that various unsteady aerodynamic theories and various types of coupling between the degrees of freedom could be accommodated. Kato and Yamane calculate the rotor impedence of articulated-rotor helicopters in hover (1979a) and forward flight (1979b) using a quasisteady approximation that neglects the effects of preceding and returning wakes. In trying to correlate their theoretical results with experiments, Kato and Yamane (1981) find that the quasisteady theory does not predict the amplitude peaks and clefts which appear near the multiples of the blade passage frequency $b\Omega$ (where b is the number of blades) whereas an analysis with Loewy's function agrees fairly well with the experiment. Various dynamic inflow models are included in a flap-lag stability analysis of a rigid blade in forward flight by Peters and Gaonkar (1980). Their study concludes that unsteady perturbations in the induced flow have a significant effect on both the flap and lead-lag damping, particularly for the regressing mode.

The application of the present method consists of two parts. First, numerical results are obtained for uniform single-load-path blades. Results are compared

with that of a previous research based on a modal method. Comparisons with experimental results are also made. The second part of the application concerns multiple-load-path blades. The formulation made for single-load-path blades is modified here to include the multibeams of the root flexure of bearingless blades. Each of the flexbeams and the torque tube are modelled as individual beams. The displacement compatibility conditions, at the clevis, between the inboard beams and the outboard beam are used in the modelling of the bearingless blade. Refined finite elements with internal nodes are used. Numerical results are obtained for several analytical models of the bearingless blade in hover. To determine the accuracy of the conventional equivalent-beam approaches, results are obtained for a blade with equivalent properties. Comparisons are made between the results of the present and equivalent-beam models.

This is the first attempt to solve the nonlinear trim equations of a flap-lag-torsion rotor blade using the finite element analysis directly. This approach enables the coupled natural rotaing modes to be calculated about the steady deflected positon of the blade. This is the first research to apply the finite element method to bearingless blades; and the first one to model the multibeams of the flexure individually.

2. HAMILTON'S PRINCIPLE FORMULATION

2.1 Coordinate Systems

The coordinate systems used are shown in Fig. 4. The rotor blade is treated as an elastic beam rotating at constant angular velocity Ω. The rectangular coordinate system x, y, z is attached to the undeformed blade which is at a precone angle of β_p. The origin is at the root of the blade, the x axis coincides with the elastic axis, and the y axis is in the plane of rotation pointed towards the leading edge. The deformed position of the blade is defined as follows. A point P on the undeformed elastic axis undergoes displacements u, v, w in the x, y, z directions, respectively, and occupies the position P' on the deformed elastic axis; u is the axial deflection, v the lead-lag deflection, and w the flap deflection. Then the blade cross section containing P' undergoes a rotation θ_1 about the deformed elastic axis. The orientation of the deformed-beam cross section with respect to the undeformed-beam cross section is described by a sequence of three rotations. This analysis uses the lag-flap-pitch sequence of rotations defined in Hodges, Ormiston and Peters (1980). The thrid angle in the sequence, θ_1, is written as

$$\theta_1 = \theta + \hat{\phi} \tag{2.1}$$

and $\hat{\phi}$ to second order is

$$\hat{\phi} \approx \phi - \int_0^x v'' w' \, dx \tag{2.2}$$

where θ is the pretwist, $\hat{\phi}$ is the geometric twist, and ϕ is the elastic twist due to torsion. The orthogonal coordinate system ξ, η, ζ is attached to the deforemed blade

such that the ξ axis is tangential to the deflected elastic axis and the η and ς axes are the principal axes of the cross section. The transformation between the two coordinate systems is given as

$$\begin{Bmatrix} \vec{i}_\xi \\ \vec{i}_\eta \\ \vec{i}_\varsigma \end{Bmatrix} = [T] \begin{Bmatrix} \vec{i}_x \\ \vec{i}_y \\ \vec{i}_z \end{Bmatrix} \tag{2.3}$$

where $\vec{i}_\xi, \vec{i}_\eta, \vec{i}_\varsigma$ and $\vec{i}_x, \vec{i}_y, \vec{i}_z$ are the unit vector systems in the two coordinate frames. The transformation matrix is defined in Hodges et al (1980) and is reproduced in appendix *A*.

2.2 Hamilton's Principle

The formulation is based on Hamilton's principle:

$$\Delta \equiv \int_{t_1}^{t_2} (\delta U - \delta T - \delta W)\, dt = 0 \tag{2.4}$$

where δU, δT, and δW are, respectively, the variation of strain energy, the variation of kinetic energy, and the virtual work done by external forces. Hodges and Dowell (1974) give expressions for δU, and δT. The expression for the variation of the strain energy is

$$\begin{aligned}\delta U = \int_0^R \Big\langle & F\Big(\delta u' + v'\delta v' + w'\delta w'\Big) \\ & + \Big[GJ\phi' + EAk_A^2(\theta+\phi)'\Big(u' + \frac{1}{2}v'^2 + \frac{1}{2}w'^2\Big) \\ & + EB_1\theta_1'^2 - EB_2\theta_1'(v''\cos\theta_1 + w''\sin\theta_1)\Big]\delta\hat{\phi}' \\ & + [EC_1\phi'' + EC_2(w''\cos\theta_1 - v''\sin\theta_1)]\delta\hat{\phi}'' \\ & + \Big\{\Big[EI_z\Big(v''\cos\theta_1 + w''\sin\theta_1\Big) - EAe_a\Big(u' + \frac{1}{2}v'^2 + \frac{1}{2}w'^2\Big) - EB_2\theta'\phi'\Big]\cos\theta_1 \\ & + \Big[EI_y\Big(v''\sin\theta_1 - w''\cos\theta_1\Big) - EC_2\phi''\Big]\sin\theta_1\Big\}\Big(\delta v'' + w''\delta\hat{\phi}\Big) \\ & + \Big\{\Big[EI_z\Big(v''\cos\theta_1 + w''\sin\theta_1\Big) - EAe_a\Big(u' + \frac{1}{2}v'^2 + \frac{1}{2}w'^2\Big) - EB_2\theta'\phi'\Big]\sin\theta_1 \\ & - \Big[EI_y\Big(v''\sin\theta_1 - w''\cos\theta_1\Big) - EC_2\phi''\Big]\cos\theta_1\Big\}\Big(\delta w'' - v''\delta\hat{\phi}\Big)\Big\rangle\, dx \end{aligned} \tag{2.5}$$

where the axial force F is defined by

$$F = EA\Big[u' + \frac{1}{2}v'^2 + \frac{1}{2}w'^2 + k_A^2\theta'\phi' - e_a(v''\cos\theta_1 + w''\sin\theta_1)\Big] \tag{2.6}$$

and the section constants are

$$
\begin{aligned}
A &\equiv \int\int_A d\eta\, d\zeta \\
Ae_a &\equiv \int\int_A \eta\, d\eta\, d\zeta \\
I_y &\equiv \int\int_A \zeta^2\, d\eta\, d\zeta \\
I_z &\equiv \int\int_A \eta^2\, d\eta\, d\zeta \\
Ak_A^2 &\equiv \int\int_A \left(\eta^2 + \zeta^2\right) d\eta\, d\zeta \\
J &\equiv \int\int_A \left[\left(\eta - \frac{\partial\lambda}{\partial\zeta}\right)^2 + \left(\zeta + \frac{\partial\lambda}{\partial\eta}\right)^2\right] d\eta\, d\zeta \\
B_1 &\equiv \int\int_A \left(\eta^2 + \zeta^2\right) d\eta\, d\zeta \\
B_2 &\equiv \int\int_A \eta\left(\eta^2 + \zeta^2\right) d\eta\, d\zeta \\
C_1 &\equiv \int\int_A \lambda^2\, d\eta\, d\zeta \\
C_2 &\equiv \int\int_A \zeta\lambda\, d\eta\, d\zeta
\end{aligned}
\tag{2.7}
$$

The blade cross-section area effective in carrying tension is A. I_y and I_z are, respectively, the flapwise and chordwise area moments of inertia of the cross section; Ak_A^2 is the polar moment of inertia of the cross section; J is the torsional constant including cross-section warping; e_a is the offset of the tension axis from the elastic axis, positive forward; B_1, B_2, C_1, and C_2 are other section constants; λ is the warp function which is assumed to be antisymmetric about the chord. The cross section is assumed to be symmetric about the chord.

The variation of the kinetic energy for the elastic beam is

$$
\begin{aligned}
\delta T = \int_0^R \Big\{ & m\Big(\Omega^2 x + 2\Omega\dot{v} - \ddot{u}\Big)\delta u \\
& + \Big[m\Omega^2(v + e_g\cos\theta_1) + 2m\Omega(\beta_p\dot{w} - \dot{u}) \\
& + 2me_g\Omega\Big(\dot{v}'\cos\theta_1 + \dot{w}'\sin\theta_1\Big) - m\ddot{v} + me_g\ddot{\hat{\phi}}\sin\theta_1\Big]\delta v \\
& - \Big[m\beta_p\Big(\Omega^2 x + 2\Omega\dot{v}\Big) + mw + me_g\ddot{\hat{\phi}}\cos\theta_1\Big]\delta w \\
& - \Big[mk_m^2\ddot{\hat{\phi}} + m\Omega^2\Big(k_{m_2}^2 - k^2 m_1\Big)\cos\theta_1\sin\theta_1 \\
& + me_g\Omega^2 x(w'\cos\theta_1 - v'\sin\theta_1) + me_g\Omega^2 v\sin\theta_1 \\
& + me_g\Omega^2\beta_p x\cos\theta_1 - me_g(\ddot{v}\sin\theta_1 - \ddot{w}\cos\theta_1)\Big]\delta\hat{\phi} \\
& - me_g\Big(\Omega^2 x\cos\theta_1 + 2\Omega\dot{v}\cos\theta_1\Big)\delta v' \\
& - me_g\Big(\Omega^2 x\sin\theta_1 + 2\Omega\dot{v}\sin\theta_1\Big)\delta w'\Big\}\, dx
\end{aligned}
\tag{2.8}
$$

Where the section integrals are defined by

$$
\begin{aligned}
m &\equiv \int\int_A \rho\, d\eta\, d\zeta \\
me_g &\equiv \int\int_A \rho\eta\, d\eta\, d\zeta \\
mk_{m_1}^2 &\equiv \int\int_A \rho\zeta^2\, d\eta\, d\zeta \\
mk_{m_2}^2 &\equiv \int\int_A \rho\eta^2\, d\eta\, d\zeta \\
k_m^2 &= k_{m_1}^2 + k_{m_2}^2
\end{aligned}
\tag{2.9}
$$

The blade mass per unit length is m; e_g is the center of mass offset from the elastic axis, positive forward; and k_{m_1} and k_{m_2} are the flapwise and chordwise mass moments of inertia per unit length.

The virtual work δW of the external forces may be expressed as

$$\delta W = \int_0^R \left(L_u \delta u + L_v \delta v + L_w \delta w + M_\phi \delta \psi \right) dx \tag{2.10}$$

where L_u, L_v, L_w, and M_ϕ are the external loads distributed along the length of the blade in the axial, lead-lag, flap, and torsion directions respectively and the virtual rotation $\delta\psi$ as defined in Hodges et al (1983) is

$$\delta\psi \approx \delta\hat{\phi} + w'\delta v' \tag{2.11}$$

Since δU, δT, and δW, as given in Eqs. (2.5), (2.8), and (2.10), are independent of the time derivatives of δu, δv, δw, and $\delta\hat{\phi}$, Eq. (2.4) can be written as

$$\Delta \equiv \delta U - \delta T - \delta W = 0 \tag{2.12}$$

2.3 Elimination of the Axial Displacement

For single load path blades, the axial displacement u can be eliminated in terms of the other deflections v, w, and ϕ and the centrifugal force F. This is possible only for single-load-path blades since the force equilibrium equation in the axial direction can be solved a priori.

Equation (2.12) would result in four equations of motion representing δu, δv, δw, and $\delta\hat{\phi}$, respectively. The δu equation is

$$\int_0^R \left[-F\delta u' + \left(m\Omega^2 x + 2m\Omega\dot{v} + L_u \right) \delta u \right] dx = 0 \tag{2.13}$$

Integrating by parts and noting that

$$\delta u = 0 \qquad at \quad x = 0$$

and

$$F = 0 \qquad at \quad x = R,$$

the above equation can be written as

$$\int_0^R \left(F' + m\Omega^2 x + 2m\Omega\dot{v} + L_u\right)\delta u \, dx = 0 \tag{2.14}$$

Since this equation is true for arbitrary values of δu,

$$F' + m\Omega^2 x + 2m\Omega\dot{v} + L_u = o \tag{2.15}$$

The external loads are of aerodynamic origin and the radial drag force L_u is negligible in hover. So neglecting L_u and integrating Eq. (2.15) results in

$$F(x) = \int_x^R m\left(\Omega^2 x + 2\Omega\dot{v}\right) dx \tag{2.16}$$

The displacement u is eliminated from δU, δT, and δW using Eqs. (2.6) and (2.16).

2.4 Nondimensionalisation

After eliminating u, the δU, δT, and δW are nondimensionalised by dividing the expressions by $m_0\Omega^2 R^3$, where m_0 is a reference mass per unit length (for example,

the value of m at $0.5R$). This is done to see the relative order of magnitude of each term. The nondimensional displacements v/R, w/R, and ϕ are assumed to be of order ϵ where ϵ is a small nondimensional quantity such that $\epsilon^2 \ll 1$. The other nondimensional quanities and their assumed orders of magnitude are given in Appendix *B*. The lowest order (i.e, first order) terms in δU and δT are of order ϵ^2. Terms of order ϵ^2 and ϵ^3 are retained while neglecting all terms of order ϵ^4 (i.e., third order) and higher, excepting some linear third order terms which are important for the torsion equation. The following simplified nondimensional expressions for δU, and δT, and δW result. The symbols are retained after nondimensionalisation.

$$
\begin{aligned}
\frac{\delta U}{m_0\Omega^2R^3} = \int_0^1 \Big\langle & F\Big(v'\delta v' + w'\delta w'\Big) \\
& + GJ\Big(\hat{\phi}'\delta\hat{\phi}' + \hat{\phi}'w'\delta v'' + \hat{\phi}'v''\delta w' + v''w'\delta\hat{\phi}'\Big) \\
& + \Big[Fk_A^2\Big(\theta' + \underline{\hat{\phi}'}\Big) - \underline{EAk_A^4\theta'^2\phi' + EAe_ak_A^2\theta'(v''\cos\theta_1 + w''\sin\theta_1)} \\
& + \underline{\underline{EB_1\theta'^2\hat{\phi}'}} - EB_2\theta'(v''\cos\theta_1 + w''\sin\theta_1)\Big]\delta\hat{\phi}' \\
& + \Big[\underline{\underline{EC_1\hat{\phi}''}} + EC_2(w''\cos\theta_1 - v''\sin\theta_1)\Big]\delta\hat{\phi}'' \\
& + \Big[-Fe_a\cos\theta_1 + \Big\{EI_z\cos^2\Big(\theta + \underline{\hat{\phi}}\Big) + EI_y\sin^2\Big(\theta + \underline{\hat{\phi}}\Big)\Big\}v'' \\
& + \frac{1}{2}(EI_z - EI_y)w''\sin 2\theta_1 - EAe_a^2\Big(v''\cos^2\theta_1 + \frac{1}{2}w''\sin 2\theta_1\Big) \\
& + \Big(\underline{EAe_ak_A^2} - EB^2\Big)\theta'\hat{\phi}'\cos\theta_1 - EC_2\hat{\phi}''\sin\theta_1\Big]\delta v'' \\
& + \Big[-Fe_a\sin\theta_1 + \Big\{EI_z\sin^2\Big(\theta + \underline{\hat{\phi}}\Big) + EI_y\cos^2\Big(\theta + \underline{\hat{\phi}}\Big)\Big\}w'' \\
& + \frac{1}{2}(EI_z - EI_y)v''\sin 2\theta_1 - EAe_a^2\Big(w''\sin^2\theta_1 + \frac{1}{2}v''\sin 2\theta_1\Big) \\
& + \Big(EAe_ak_A^2 - Eb^2\Big)\theta'\hat{\phi}'\sin\theta_1 - EC_2\hat{\phi}''\cos\theta_1\Big]\delta w'' \\
& + \Big[Fe_a\Big(v''\sin\theta_1 - w''\cos\theta_1\Big) \\
& + \underline{(EI_z - EI_y)\Big\{\frac{1}{2}\Big(w''^2 - v''^2\Big)\sin 2\theta_1 + v''w''\cos 2\theta_1\Big\}}\Big]\delta\hat{\phi}\Big\rangle\, dx
\end{aligned}
\tag{2.17}
$$

$$\frac{\delta T}{m_0\Omega^2R^3} = \int_0^1 m\Big\{\Big[v + e_g\cos\theta_1 + 2\beta_p\dot{w} + 2\int_0^x (\dot{v}v' + \dot{w}w')\,dx$$
$$+ 2e_g(\dot{v}'\cos\theta_1 + \dot{w}'\sin\theta_1) - \ddot{v} + e_g\ddot{\phi}\sin\theta_1\Big]\delta v$$
$$- \Big[\beta_p(x + 2\dot{v}) + \ddot{w} + e_g\ddot{\phi}\cos\theta_1\Big]\delta w$$
$$- \Big[k_m^2\ddot{\phi} + \frac{1}{2}\big(k_{m2}^2 - k_{m1}^2\big)\sin 2\theta_1 + e_g x(w'\cos\theta_1 - v'\sin\theta_1)$$
$$+ e_g v\sin\theta_1 + e_g\beta_p x\cos\theta_1 - e_g\Big(\ddot{v}\sin\theta_1 - \ddot{w}\cos\theta_1\Big)\Big]\delta\phi$$
$$- e_g\Big(x\cos\theta_1 + 2\dot{v}\cos\theta_1\Big)\delta v'$$
$$- e_g\Big(x\sin\theta_1 + 2\dot{v}\sin\theta_1\Big)\delta w'\Big\}\,dx \qquad (2.18)$$

and

$$\frac{\delta W}{m_0\Omega^2R^3} = \int_0^1 \left(L_v\delta v + L_w\delta w + M_\phi\delta\psi\right)dx \qquad (2.19)$$

The singly underlined terms are nonlinear and the doubly underlined terms are third order (ϵ^4) linear torsion terms.

3. AERODYNAMIC LOADS

The external loads L_v, L_w, and M_ϕ of Eq. (2.19) are of aerodynamic origin. The expressions for these aerodynamic loads in hover, distributed along the length of the blade, are obtained based on a quasisteady strip-theory approximation. The flow is assumed to be incompressible and inviscid. The induced inflow is assumed to be uniform and steady. Virtual inertia effects are included. The variation in free stream velocity due to flap, lead-lag, and torsion motions are taken into account. Blade angle-of-attack stall is neglected.

3.1 Circulatory Forces

The forces L_v and L_w are in the y and z directions respectively (i.e., in the undeformed coordinate frame). In the present analysis the strip theory is based on sections in the deformed frame. As a result, forces obtained in the deformed frame have to be transformed to the undeformed frame. The magnitude and direction of the relative wind over the blade section is obtained by vectorially adding the negative of the blade velocity to the induced inflow.

$$\vec{V} = -\vec{V}_b + \vec{v}_i \tag{3.1}$$

where $\vec{V}$ is the relative wind, $\vec{V}_b$ the blade velocity, and $\vec{v}_i$ the inflow velicity. Hodges and Dowell (1974) present the expression for $\vec{V}_b$ in terms of the unit vectors in the undeformed frame.

$$\begin{aligned}\vec{V}_b = &\left(\dot{x}_1 - \Omega y_1 \cos\beta_p\right)\vec{i}_x + \left[\dot{y}_1 + \left(x_1 \cos\beta_p - z_1 \sin\beta_p\right)\right]\vec{i}_y \\ &+ \left(\dot{z}_1 + \Omega y_1 \sin\beta_p\right)\vec{i}_z\end{aligned} \tag{3.2}$$

with

$$\begin{aligned} x_1 &= x + u - \lambda\phi' - v'(\eta\cos\theta_1 - \varsigma\sin\theta_1) - w'(\eta\sin\theta_1 + \varsigma\cos\theta_1) \\ y_1 &= v + \eta\cos\theta_1 - \varsigma\sin\theta_1 \\ z_1 &= w + \eta\sin\theta_1 + \varsigma\cos\theta_1 \end{aligned} \tag{3.3}$$

The following approximations are made.

(*a*) $\vec{V}$ is obtained at a reference point $(\eta_r,0)$ on the chord.

(*b*) $\sin\beta_p \approx \beta_p$; $\cos\beta_p \approx 1$.

(*c*) Terms of order ϵ^3 and higher are neglected.

Then Eq. (3.1) is written as

$$\vec{V} = U_x\vec{i}_x + U_y\vec{i}_y + U_z\vec{i}_z \tag{3.4}$$

where

$$\begin{aligned} U_x &= -\dot{u} + \dot{v}'\eta_r\cos\theta_1 + \dot{w}'\eta_r\sin\theta_1 + \Omega(v + \eta_r\cos\theta_1) - v_i\beta_p \\ U_y &= -\dot{v} + \dot{\phi}\eta_r\sin\theta_1 - \Omega(x + u - v'\eta_r\cos\theta_1 - w'\eta_r\sin\theta_1) + \Omega\beta_p(w + \eta_r\sin\theta_1) \\ U_z &= -\dot{w} + \dot{\phi}\eta_r\cos\theta_1 - \Omega\beta_p(v + \eta_r\cos\theta_1) - v_i \end{aligned} \tag{3.5}$$

We are interested in expressing $\vec{V}$ in the deformed frame since the airfoil section is considered in that frame. So if $\vec{V}$ is written as

$$\vec{V} = -U_R\vec{i}_\xi - U_T\vec{i}_\eta - U_p\vec{i}_\varsigma \tag{3.6}$$

Then

$$\begin{Bmatrix} -U_R \\ -U_T \\ -U_P \end{Bmatrix} = [T] \begin{Bmatrix} U_x \\ U_y \\ U_z \end{Bmatrix} \tag{3.7}$$

The axial velocity U_R is negligible in hover; the expressions for U_T and U_P are

$$\begin{aligned} U_T = {} & \Omega x\left[\left(1-\frac{1}{2}v'^2\right)\cos\theta_1 - v'w'\sin\theta_1\right] \\ & + \Omega\left[u\cos\theta_1 + (vv' - w\beta_p)\cos\theta_1 + (w'+\beta_p)v\sin\theta_1\right] \\ & + \dot{v}\cos\theta_1 + (\dot{w}+v_i)\sin\theta_1 \end{aligned} \tag{3.8}$$

and

$$\begin{aligned} U_P = {} & -\Omega x\left[\left(1-\frac{1}{2}v'^2\right)\sin\theta_1 + v'w'\cos\theta_1\right] \\ & + \Omega\left[-u\sin\theta_1 - (vv' - w\beta_p)\sin\theta_1 + (w'+\beta_p)(\eta_r + v\cos\theta_1)\right] \\ & - \dot{v}\sin\theta_1 + (\dot{w}+v_i)\cos\theta_1 + \eta_r\dot{\phi} \end{aligned} \tag{3.9}$$

According to the quasisteady approximation of the thin airfoil theory, the circulatory forces are based on the angle of attack at the three-quarter-chord point [*e.g.*, see Fung (1969) pp. 193]. Therefore U_T and U_P are evaluated at the three quarter chord point; that is, η_r is the η coordinate of the three-quarter-chord point.

Figure 5 shows the aerodynamic environment in the deformed frame. The circulatory forces L_{v_c}, L_{w_c}, and M_{ϕ_c} in the η, ζ, and ϕ directions, respectively, can be written as

$$\begin{aligned} L_{vc} &= L\sin\alpha - D\cos\alpha \\ L_{wc} &= -L\cos\alpha - D\sin\alpha \\ M_{\phi c} &= M_{ac} - L_{wc}e_d \end{aligned} \tag{3.10}$$

where L, D, and M_{ac} are, respectively, the lift, drag and pitching moment (about the aerodynamic center) per unit length, α is the angle of attack at the three-quarter-chord point, and e_d is the aerodynamic center offset from the elastic axis. The expressions for L, D, and M_{ac} are

$$\begin{aligned} L &= C_L\frac{1}{2}\rho V^2 c \\ D &= C_D\frac{1}{2}\rho V^2 c \\ M_{ac} &= C_{Mac}\frac{1}{2}\rho V^2 c^2 \end{aligned} \tag{3.11}$$

with

$$V^2 = U_T^2 + U_P^2$$

and

$$\tan\alpha = \frac{U_P}{U_T}$$

where C_L, C_D, and C_{Mac} are the section lift, drag, and pitching moment coefficients, and c is the section chord. Substituting Eqs. (3.11) in Eqs. (3.10) yields

$$
\begin{aligned}
L_{vc} &= \frac{1}{2}\rho c(C_L U_P V - C_D U_T V) \\
L_{wc} &= -\frac{1}{2}\rho c(C_L U_T V + C_D U_P V) \\
M_{\phi c} &= \frac{1}{2}\rho c^2 C_{Mac} V^2 - e_d L_{wc}
\end{aligned}
\tag{3.12}
$$

With the assumptions

$$
\begin{aligned}
C_L &= c_0 + c_1\alpha \\
C_D &= d_0 + d_1\alpha + d_2\alpha^2 \\
\alpha &\approx \sin\alpha = \frac{U_P}{V} \\
V &\approx U_T
\end{aligned}
\tag{3.13}
$$

Eqs. (3.12) can be written as

$$
\begin{aligned}
L_{vc} &= \frac{1}{2}\rho c\left[-d_0 U_T^2 + (c_0 - d_1)U_T U_P + (c_1 - d_2)U_P^2\right] \\
L_{wc} &= -\frac{1}{2}\rho c\left[c_0 U_T^2 + (c_1 + d_0)U_T U_P + d_1 U_P^2\right] \\
M_{\phi c} &= \frac{1}{2}\rho c^2 C_{Mac}\left(U_T^2 + U_P^2\right) - e_d L_{wc}
\end{aligned}
\tag{3.14}
$$

The assumed order of magnitude is unity for c_1 and d_2; ϵ for c_0, d_1, C_{Mac}, and α; $\epsilon^{3/2}$ for e_d; and ϵ^2 for d_0. The circulatory forces L_{vc} and L_{wc} in the undeformed frame are obtained from L_{vc} and L_{wc} using the transformation matrix.

$$
\begin{Bmatrix} L_{uc} \\ L_{vc} \\ L_{wc} \end{Bmatrix} = [T]^T \begin{Bmatrix} 0 \\ L_{vc} \\ L_{wc} \end{Bmatrix}
\tag{3.15}
$$

Thus, the circulatory aerodynamic force components to order ϵ^2 are

$$
\begin{aligned}
L_{vc} = \frac{1}{2}\rho c\Big\langle & \cos\theta_1\Big\{-d_0\Omega^2x^2\cos^2\theta_1+(c_0-d_1)\Big(-\frac{1}{2}\Omega^2x^2\sin 2\theta_1+\Omega x v_i\cos 2\theta_1\Big)\\
& +(c_1-d_2)\Big[(\Omega x\sin\theta_1-v_i\cos\theta_1)^2-2\Omega^2x\eta_r\beta_p\sin\theta_1\Big]\Big\}\\
& +\sin\theta_1\Big\{c_0\Big(\Omega^2x^2\cos^2\theta_1+\Omega x v_i\sin 2\theta_1\Big)\\
& +(c_1+d_0)\Big[\Omega x\cos\theta_1(-\Omega x\sin\theta_1+v_i\cos\theta_1+\Omega\eta_r\beta_p)-\Omega x v_i\sin^2\theta_1+\frac{1}{2}v_i^2\sin 2\theta_1\Big]\\
& +d_1\Big(\Omega^2x^2\sin^2\theta_1-\Omega x v_i\sin 2\theta_1\Big)\Big\}\\
& -u\Omega^2x(d_0+d_2)\sin 2\theta_1\sin\theta_1\\
& -v\Omega^2x\beta_p[(c_1-d_2)\sin 2\theta_1\cos\theta_1+(c_1+d_0)\sin\theta_1\cos 2\theta_1]\\
& +w\Omega^2x\beta_p(d_0+d_2)\sin 2\theta_1\sin\theta_1\\
& +w'\Omega^2x\eta_r(-c_1+d_0+2d_2)\sin\theta_1\cos\theta_1\\
& +\dot v\Big\{\cos\theta_1\Big[\underline{\underline{-2\Omega x d_0\cos^2\theta_1}}-\Omega x(c_0-d_1)\sin 2\theta_1+(c_1-d_2)\Big(2\Omega x\sin^2\theta_1-v_i\sin 2\theta_1\Big)\Big]\\
& +\sin\theta_1\Big[2\Omega x c_0\cos^2\theta_1-(c_1+d_0)(\Omega x\sin 2\theta_1-v_i\cos 2\theta_1)+2\Omega x d_1\sin^2\theta_1\Big]\Big\}\\
& +\dot w\Big\{\cos\theta_1\Big[\underline{\underline{-\Omega x d_0\sin 2\theta_1}}+\Omega x(c_0-d_1)\cos 2\theta_1+(c_1-d_2)\Big(-\Omega x\sin 2\theta_1+2v_i\cos^2\theta_1\Big)\Big]\\
& +\sin\theta_1\Big[\Omega x c_0\sin 2\theta_1+(c_1+d_0)\Big(\Omega x\cos 2\theta_1+v_i\sin 2\theta_1\Big)-\Omega x d_1\sin 2\theta_1\Big]\Big\}\\
& +\dot\phi\Omega x\eta_r(-c_1+d_0+2d_2)\sin\theta_1\cos\theta_1\\
& -\underline{v v'\Omega^2x(d_0+d_2)\sin\theta_1\sin 2\theta_1}\\
& -\underline{v w'\Omega^2x[-(c_1-d_2)\sin 2\theta_1\cos\theta_1+(c_1+d_0)\sin\theta_1\cos 2\theta_1]}\\
& -\underline{v'^2\Omega^2x^2\frac{3}{2}(d_0+d_2)\sin^2\theta_1\cos\theta_1}\\
& -\underline{v'w'\Omega^2x^2\Big[(c_1-d_2)\Big(\sin 2\theta_1\cos\theta_1-\sin^3\theta_1\Big)}\\
& +\underline{(c_1+d_0)\Big(-\sin 2\theta_1\cos\theta_1+\sin^3\theta_1\Big)\Big]}\Big\rangle
\end{aligned}
\tag{3.16}
$$

$$
\begin{aligned}
L_{wc} = \frac{1}{2}\rho c\Big\langle & \sin\theta_1\Big\{-d_0\Omega^2x^2\cos^2\theta_1+(c_0-d_1)\Big(-\frac{1}{2}\Omega^2x^2\sin 2\theta_1+\Omega x v_i\cos 2\theta_1\Big)\\
& +(c_1-d_2)\Big[(\Omega x\sin\theta_1-v_i\cos\theta_1)^2-2\Omega^2x\eta_r\beta_p\sin\theta_1\Big]\Big\}\\
& -\cos\theta_1\Big\{c_0\Big(\Omega^2x^2\cos^2\theta_1+\Omega x v_i\sin 2\theta_1\Big)\\
& +(c_1+d_0)\Big[\Omega x\cos\theta_1(-\Omega x\sin\theta_1+v_i\cos\theta_1+\Omega\eta_r\beta_p)-\Omega x v_i\sin^2\theta_1+\frac{1}{2}v_i^2\sin 2\theta_1\Big]\\
& +d_1\Big(\Omega^2x^2\sin^2\theta_1-\Omega x v_i\sin 2\theta_1\Big)\Big\}\\
& -u\,2\Omega^2x\Big[(c_1-d_2)\sin^3\theta_1+(c_1+d_0)\sin\theta_1\cos^2\theta_1\Big]\\
& -v\Omega^2x\beta_p[(c_1-d_2)\sin\theta_1\sin 2\theta_1+(c_1+d_0)\cos\theta_1\cos 2\theta_1]\\
& -w\,2\Omega^2x\beta_p\Big[(c_1-d_2)\sin^3\theta_1+(c_1+d_0)\sin\theta_1\cos^2\theta_1\Big]\\
& -w'\Omega^2x\eta_r\Big[2(c_1-d_2)\sin^2\theta_1+(c_1+d_0)\cos^2\theta_1\Big]\\
& +\dot v\Big\{\sin\theta_1\Big[\underline{\underline{-2\Omega x d_0\cos^2\theta_1}}-\Omega x(c_0-d_1)\sin 2\theta_1+(c_1-d_2)\Big(2\Omega x\sin^2\theta_1-v_i\sin 2\theta_1\Big)\Big]\\
& -\cos\theta_1\Big[2\Omega x c_0\cos^2\theta_1-(c_1+d_0)(\Omega x\sin 2\theta_1-v_i\cos 2\theta_1)+2\Omega x d_1\sin^2\theta_1\Big]\Big\}\\
& +\dot w\Big\{\sin\theta_1\Big[\underline{\underline{-\Omega x d_0\sin 2\theta_1}}+\Omega x(c_0-d_1)\cos 2\theta_1+(c_1-d_2)\Big(-\Omega x\sin 2\theta_1+2v_i\cos^2\theta_1\Big)\Big]\\
& -\cos\theta_1\Big[\Omega x c_0\sin 2\theta_1+(c_1+d_0)\Big(\Omega x\cos 2\theta_1+v_i\sin 2\theta_1\Big)-\Omega x d_1\sin 2\theta_1\Big]\Big\}\\
& -\dot\phi\Omega x\eta_r\Big[2(c_1-d_2)\sin^2\theta_1+(c_1+d_0)\cos^2\theta_1\Big]\\
& -\underline{v v'\Omega^2x\Big[2(c_1-d_2)\sin^3\theta_1+(c_1+d_0)\sin 2\theta_1\cos\theta_1\Big]}\\
& -\underline{v w'\Omega^2x[(c_1-d_2)\sin\theta_1\sin 2\theta_1+(c_1+d_0)\cos\theta_1\cos 2\theta_1]}\\
& -\underline{v'^2\Omega^2x^2\Big[(c_1-d_2)\sin^3\theta_1+(c_1+d_0)\sin\theta_1\cos^2\theta_1\Big]}\\
& +\underline{v'w'\Omega^2x^2[(c_1-d_2)\sin\theta_1\sin 2\theta_1+(c_1+d_0)\cos\theta_1\cos 2\theta_1]}\\
& -\underline{w'^2\Omega^2x^2\frac{1}{2}\Big[(c_1-d_2)\sin^3\theta_1+(c_1+d_0)\sin\theta_1\cos^2\theta_1\Big]}\Big\rangle
\end{aligned}
\tag{3.17}
$$

$$M_{\phi c} = \frac{1}{2}\rho c\Big\langle \Omega^2 x^2 \Big\{ cC_{Mac} - e_d\Big[(c_1 + d_0)\sin\theta_1\cos\theta_1 - d_1\sin^2\theta_1\Big]\Big\} - \Omega x e_d(c_1 + d_0)\Big(\dot{v}\sin 2\theta_1 - \dot{w}\cos 2\theta_1\Big)\Big\rangle \tag{3.18}$$

The singly underlined terms are nonlinear and the doubly underlined terms are third order damping terms.

3.2 Noncirculatory Forces

The noncirculatory components are obtained from unsteady thin airfoil theory [Fung (1969), pp 209-210]. To order ϵ^2, they are

$$\begin{aligned} L_{wnc} &= \frac{1}{4}\pi\rho c^2\Big[-\ddot{w} + \Omega x\dot{\phi} + \Big(\frac{1}{4}c + e_d\Big)\ddot{\phi}\Big] \\ M_{\phi nc} &= \frac{1}{4}\pi\rho c^2\Big[\Big(\frac{1}{4}c + e_d\Big)\ddot{w} - \Big(\frac{1}{2}c + e_d\Big)\Omega x\dot{\phi}\Big] \end{aligned} \tag{3.19}$$

3.3 Combined Forces

The expressins for the complete aerodynamic forces in the lead-lag, flap, and torsion directions are given by

$$\begin{aligned} L_v &= L_{vc} \\ L_w &= L_{wc} + L_{wnc} \\ M_\phi &= M_{\phi c} + M_{\phi nc} \end{aligned} \tag{3.20}$$

In the derivation of the above aerodynamic forces, nonlinear rate product terms such as $\dot{v}^2$, $\dot{w}^2$, $\dot{v}\dot{w}$ are neglected while retaining other nonlinear terms up to order ϵ^2. This is necessary for a linearized perturbation analysis about the steady state.

Some damping terms of order ϵ^3, which may be important for the stability analysis, are retained. The uniform induced velocity is based on the momentum theory. The pitch of the blade is obtained by combining the momentum and blade element theories.

$$\begin{aligned} \lambda_i &= k_h\sqrt{\frac{C_T}{2}} \\ \theta_{.75R} &= \frac{6C_T}{\sigma a} + 1.5\lambda_i \end{aligned} \tag{3.21}$$

where k_h is an empircal factor, C_T the thrust coefficient, σ the solidity ratio of the rotor, and $\theta_{.75R}$ the blade pitch at three-quarter span.

4. FINITE ELEMENT DISCRETIZATION

4.1 Equations of Motion in Terms of Nodal Degrees of Freedom

The finite element analysis is used to discretize the spatial dependence of the equations of motion. The blade is divided into a number of beam elements. Every element consists of two nodes, denoted by node-1 and node-2 (Fig. 6), with five degrees of freedom namely v, v', w, w', and $\hat{\phi}$ at each node. The reason for choosing $\hat{\phi}$ over ϕ as the torsional degree of freedom is as follows. The aerodynamic loads depend explicitly on $\hat{\phi}$. If ϕ is chosen as the torsional degree of freedom, then the presence of the integral term $\int_0^x v''w'\,dx$ [Eq. (2.2)] makes the global matrices nonbanded because of the coupling of the degrees of freedom of one element with that of the other elements. The choice of $\hat{\phi}$ eliminates this integral and thus preserves the banded structure of the global matrices.

Hamilton's principle, Eq. (2.12), is discretized as

$$\Delta \equiv \sum_{i=1}^{n} \Delta_i = 0 \tag{4.1}$$

with

$$\Delta_i \equiv \delta U_i - \delta T_i - \delta W_i \tag{4.2}$$

where δU_i, δT_i, and δW_i are respectively the strain energy, kinetic energy, and the virtual work contributions of the ith element and n is the total number of elements. The distribution of the deflections v, w, $\hat{\phi}$ over an element is represented in terms of the nodal displacements using shape functions. For the ith element (Fig. 6),

$$\begin{Bmatrix} v \\ w \\ \hat{\phi} \end{Bmatrix} = [H] \{q_i\} \tag{4.3}$$

where the shape function matrix $[H]$ is

$$[H] = \begin{bmatrix} H_1 & H_2 & H_3 & H_4 & 0 & 0 & 0 & 0 & 0 & 0 \\ 0 & 0 & 0 & 0 & H_1 & H_2 & H_3 & H_4 & 0 & 0 \\ 0 & 0 & 0 & 0 & 0 & 0 & 0 & 0 & H_{\phi_1} & H_{\phi_2} \end{bmatrix} \tag{4.4}$$

and the vector of element degrees of freedom $\{q_i\}$ is defined as

$$\{q_i\} = \lfloor v_1 \quad v_1' \quad v_2 \quad v_2' \quad w_1 \quad w_1' \quad w_2 \quad w_2' \quad \hat{\phi}_1 \quad \hat{\phi}_2 \rfloor \tag{4.5}$$

The nodal degrees of freedom at node-1 of the element are v_1, v_1', w_1, w_1', $\hat{\phi}_1$ and those at node-2 are v_2, v_2', w_2, w_2', $\hat{\phi}_2$. The shape functions in Eq. (4.4) are the Hermite polynomials defined as

$$\begin{aligned} H_1(x_i) &= 2\left(\frac{x_i}{l_i}\right)^3 - 3\left(\frac{x_i}{l_i}\right)^2 + 1 \\ H_2(x_i) &= l_i\left[\left(\frac{x_i}{l_i}\right)^3 - 2\left(\frac{x_i}{l_i}\right)^2 + \frac{x_i}{l_i}\right] \\ H_3(x_i) &= -2\left(\frac{x_i}{l_i}\right)^3 + 3\left(\frac{x_i}{l_i}\right)^2 \\ H_4(x_i) &= l_i\left[\left(\frac{x_i}{l_i}\right)^3 - \left(\frac{x_i}{l_i}\right)^2\right] \\ H_{\phi_1}(x_i) &= 1 - \frac{x_i}{l_i} \\ H_{\phi_2}(x_i) &= \frac{x_i}{l_i} \end{aligned} \tag{4.6}$$

where l_i is the length of the ith element and x_i is the local axial coordinate for the ith element, measured from the left end of the element (Fig. 6). Similar to Eq. (4.3), the distribution of the virtual displacements δv, δw, and $\delta\hat{\phi}$ over the ith element is assumed to be

$$\begin{Bmatrix} \delta v \\ \delta w \\ \delta\hat{\phi} \end{Bmatrix} = [H] \{\delta q_i\} \tag{4.7}$$

The substitution of Eq. (4.3) and Eq. (4.7) in Eq. (4.2) results in

$$\Delta_i = f(\ddot{q}_i, \dot{q}_i, q_i, \delta q_i) \tag{4.8}$$

which is nonlinear in q_i. This function can be conveniently written as

$$\begin{aligned} \Delta_i = {} & \{\delta q_i\}^T [M_i(q_i)]\{\ddot{q}_i\} + \{\delta q_i\}^T [C_i(q_i)]\{\dot{q}_i\} \\ & + \{\delta q_i\}^T [K_i(q_i)]\{q_i\} - \{\delta q_i\}^T \{Q_i\} \end{aligned} \tag{4.9}$$

where $[M_i(q_i)]$, $[C_i(q_i)]$, and $[K_i(q_i)]$, represent the element inertia, damping and stiffness matrices, respectively and $\{Q_i\}$ is the element load vector for the ith element. The global matrices are obtained by the assembly of the element matrices.

The global degree of freedom vector is denoted by $\{q\}$ and the global virtual displacement vector by $\{\delta q\}$. The global load vector $\{Q\}$ is formed by combining the element load vectors $\{Q_i\}$. The assembly of element inertia matrices $[M_i(q_i)]$ results in global inertia matrix $[M(q)]$ as shown below.

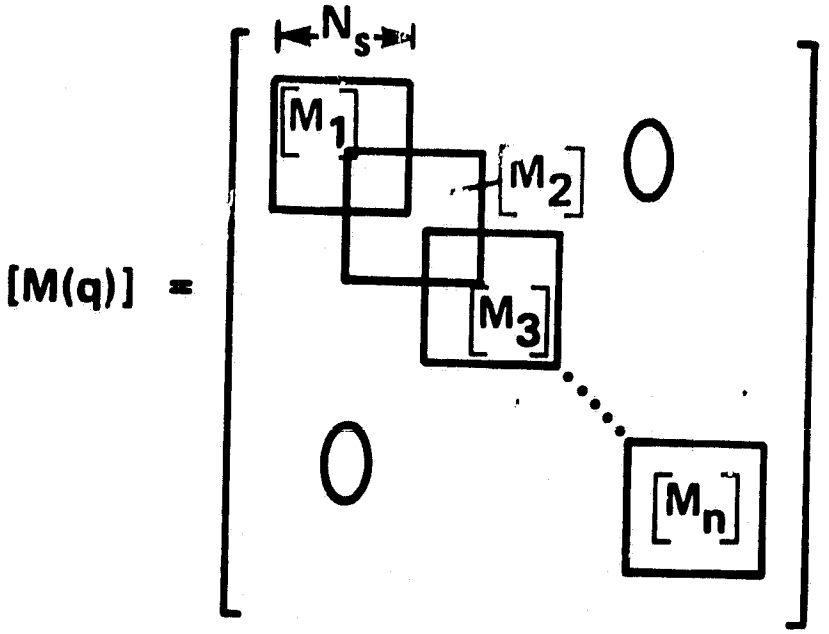

The matrix $[M]$ is a square matrix of order $5(n+1)$; it is also banded with the semibandwidth N_s equal to 10. The global damping and stifness matrices $[C(q)]$ and $[K(q)]$ are obtained in the same manner. The matrix $[K]$ also is banded, whereas the matrix $[C]$ is nonbanded because of the presence of the double integral term

$$\int_0^{l_i} \int_0^x (\dot{v}'v' + \dot{w}'w')\, dx\, dx_i$$

in the expression for δT_i [Eq. (2.18)]. Matrix $[M]$ is symmetric; the presence of terms in [C] and [K] due to the nonconservative aerodynamic forces makes them asymmetric. The process of assembling element matrices to obtain global matrices can be mathematically indicated by substituting Eq. (4.9) in Eq. (4.1).

$$\Delta = \{\delta q\}^T[M(q)]\{\ddot{q}\} + \{\delta q\}^T[C_i(q)]\{\dot{q}\} + \{\delta q\}^T[K(q)]\{q\} - \{\delta q\}^T\{Q\} = 0 \tag{4.10}$$

Since the virtual dispalcements δq are arbitrary, Eq. (4.10) leads to the equations of motion

$$[M(q)]\{\ddot{q}\} + [C(q)]\{\dot{q}\} + [K(q)]\{q\} = \{Q\} \tag{4.11}$$

These equations are nonlinear in q. The bandedness of $[M]$ and $[K]$ helps reduce the storage space needed in computer programs since the zero elements off the band need not be stored.

4.2 Boundary Conditions

The formulation of the problem is based on energy priciples; and hence, the force boundary conditions, which are imbedded in the formulation, do not have to be considered separately. The nature of the displacement boundary conditions at the root determines the configuration of the rotor. For example, v, v', w, w', and $\hat{\phi}$ are zero at the root for a hingeless rotor blade; and for an articulated blade, v, w, and $\hat{\phi}$ are zero at the hinge.

5. SOLUTION PROCEDURE

5.1 Trim Solution

The steady trim condition of the rotor in hover is determined first since the flutter stability equations are linearized about the trim state. The nonlinear steady-state equations are obtained by dropping all time-dependent terms from Eq. (4.11).

$$[K_0(q_0)]\{q_0\} = \{Q_0\} \tag{5.1}$$

The matrix $[K_0]$ is asymmetric, banded, and a function of the steady displacement q_0. The contribution to the matrices $[K_0]$ and $\{Q_0\}$ is from both structural and aerodynamic forces. The expressions for the terms of the steady-state element matrices are given in Appendix C. These matrices are evaluated numerically using Gauss quadrature formulas. The numerical solution of the nonlinear steady-state equations is evaluated iteratively using Brown's algorithm [Brown and Dennis (1972)]. This algorithm is a modified form of the Newton-Raphson method and the solution is estimated such that the sum of the squares of the errors in the equations is a minimum. The linear solution of Eqs. (5.1) is used as the initial estimate in the solution procedure. The nonlinear stiffness matrix $[K_0(q_0)]$ is updated at every step of the iteration using the estimate from the previous step. The bandedness of $[K_0]$ is useful in two ways. The storage space needed in the computer program is less since only the elements within the band are stored. The number of computer operations is reduced considerably since the matrix operations corresponding to the zero entries of $[K_0]$, outside the band, are skipped.

For a given level of thrust, the collective pitch required at three-quarter span ($\theta_{.75R}$) is calculated from Eqs. (3.18). The steady elastic twist modifies the pitch

distribution of the blade. The new pitch at three-quarter span is $\theta_{.75R} + \phi_{.75R}$ and corresponding to this pitch vallue, a new thrust level is calculated.

5.2 Flutter Stability

The flutter equations of motion are linearized about the steady-state solution. The displacement q is written as the sum of a steady component (q_0) and an unsteady perturbation ($\tilde{q}$).

$$q = q_0 + \tilde{q} \tag{5.2}$$

Substituting Eq. (5.2) into Eqs. (4.11), subtracting Eqs. (5.1), and keeping only linear perturbation terms, the flutter equations are obtained as

$$\left[\tilde{M}(q_0)\right]\left\{\ddot{\tilde{q}}\right\} + \left[\tilde{C}(q_0)\right]\left\{\dot{\tilde{q}}\right\} + \left[\tilde{K}(q_0)\right]\{\tilde{q}\} = \{0\} \tag{5.3}$$

The inertia, damping, and stiffness matrices are functions of the steady deflection q_0. The expressions for the terms of the perturbation element matrices are given in Appendix *D*.

The flutter stability is determined by studying the eigenvalues of Eqs. (5.3). The normal mode method (which considerably reduces the number of equations) is used to calculate the flutter eivenvalues; and hence the natural modes are needed. The coupled rotating vibration characteristics about the equilibrium position are evaluated by dropping the damping matrix and removing all aerodynamic terms from Eqs. (5.3). The resulting equations are

$$[M_e]\left\{\ddot{\tilde{q}}\right\} + [K_e]\{\tilde{q}\} = \{0\} \tag{5.4}$$

The inertia and stiffness matrices $[M_s]$ and $[K_s]$ are symmetric and the eigenvalues (frequencies) of Eqs. (5.4) are real.

The flutter equations of motion, Eqs. (5.3), are transformed to the modal space by writing

$$\{\tilde{q}\} = [\Phi]\{p\} \tag{5.5}$$

where $[\Phi]$ is the matrix of the first N eigenvectors (colulmnwise) and $\{p\}$ is the vector of N generalized coordinates in the modal space. Substituting Eqs. (5.5) into Eqs. (5.3) and premultiplying by $[\Phi]^T$ yields the modal-space equations

$$[M^*]\{\ddot{p}\} + [C^*]\{\dot{p}\} + [K^*]\{p\} = \{0\} \tag{5.6}$$

The matrices $[M^*]$, $[C^*]$, and $[K^*]$ are asymmetric and of order N. These equations can be written as a first order system of $2N$ equations.

$$[A]\{r\} - [B]\{r\} = \{0\} \tag{5.7}$$

where

$$[A] = \begin{bmatrix} [M^*] & [C^*] \\ [0] & [I] \end{bmatrix}$$

$$[B] = \begin{bmatrix} [0] & [K^*] \\ [I] & [0] \end{bmatrix}$$

and

$$\{r\} = \begin{Bmatrix} \{\dot{p}\} \\ \{p\} \end{Bmatrix}$$

By writing r as

$$r = \bar{r}e^{\lambda t} \tag{5.8}$$

Eqs. (5.7) becomes

$$[A]\{\bar{r}\} = \lambda[B]\{\bar{r}\} \tag{5.9}$$

These equations are solved as an algebraic eigenvalue problem. The eigenvalues λ are complex.

6. APPLICATION TO SINGLE-LOAD-PATH BLADES

To show the fesibility of the finite element formulation, the method is first applied to single-load-path blades; a hingeless blade and an articulated blade with a hinge offset of 6%are considered. Convergence studies with respect to increasing number of finite eflements and natural modes are presented. For the hingeless blade, comparisons are made with previous theoretical results obtained by modal methods and with some experimental results.

The numerical results obtained are for blades with uniform spanwise poperties. The chordwise offsets of the center of mass, aerodynamic center, and tension center from the elastic axis are considered to be zero. The section constatnts EB_1, EB_2, and the warping constants EC_1, EC_2, are taken to be zero. A precone (β_p) of 0.05 rad (2.9 deg), Lock number (γ) of 5, and solidity ratio (σ) of 0.1 are used.

6.1 Hingeless Rotor Blades

The uniform blade properties selected for the stability analysis of a hingeless rotor blade are given in Table 1. The stiffnesses EI_y, EI_z, GJ, and the inertial parameters k_{m_1}, k_{m_2}, k_A are chosen such that the rotating frequencies corresponding to given values. The rotating flap frequency of the blade is taken to be 1.15Ω. Two different lead-lag frequencies are considered; a frequency of 0.7Ω represents a soft-inplane blade whereas 1.5Ω represents a stiff-inplane blade. Similarly a torsional rotating frequency of 2.5Ω represents a torsionally-soft blade and 5Ω a torsionally-stiff blade.

The convergence of the steady state deflections using different numbers of finite elements is presented first. Table 2 shows the steady tip deflections $v_{0_{tip}}$ $w_{0_{tip}}$ (nondimensionalized with respect to the rotor length) and $\hat{\phi}_{0_{tip}}$ (in rad) as the total number of finite elements is varied from 2 to 8. The results are for a thrust level,

C_T/σ, of 0.1. The results show, for the case considered, that six elements are sufficient for good convergence (three to four digit accuracy). The banded nature of the stiffness matrix reduces both the storage space and computation time required. For example, if eight elements are used, the full storage mode would require 2025 storage locations whereas the band storage mode needs only 855 locations for the stiffness matrix. Furthermore, the number of arithmetic operations involving the stiffness matrix is reduced by about 60%. The use of the linear solution as the starting vector makes the nonlinear iterative solution converge rapidly; only three or four iterations are needed for a converged solution. As a result, the computation time required for the trim solution is small.

Figure 7 shows the steady tip deflections of a stiff-inplane hingeless blade as the thrust C_T/σ, (and hence the pitch θ) is varied. The torsion frequency corresponds to a torsionally-stiff blade for these results. The magnitue of the flap and lead-lag tip deflections increase with thrust. The magnitude of the torsional tip deflection increases first and at higher thrust levels decreases. The torsional deflection is primarily due to nonlinear flap-torsion and lag-torsion couplings. The steady-state aerodynamic torsional moment is zero since C_{Mac} and e_d are assumed to be zero [see Eq. (3.18)]. At low values of C_T/σ, both the flap and lead-lag deflections are negative. At high values, the flap deflection is positive while the lead-lag deflection is negative. The results of Hodges and Ormiston (1976) are also shown in this figure. Hodges and Ormiston use a modal method with five nonrotating beam modes for each one of the deflections v_0, w_0, and ϕ_0. The agreement between the two results is excellent except at high trust levels where a slight deviation appears. This may be due to the assumption by Hodges and Ormiston that $\sin\theta \approx \theta$ and $\cos\theta \approx 1$ (not assumed here) for the claculation of aerodynamic loads, which may not be very accurate at high values of θ. The steady tip deflections with respect to thrust for a soft-inplane blade are shown in Fig. 8. The flap, lead-lag, and torsion curves

are similar to that of the previous case. The flap deflections are almost identical to that of the stiff-inplane blade. The lead-lad deflections are higher in magnitude, as expected, since the lead-lag stiffness is lower. The torsional deflections also are higher in magnitude than for the stiff-inplane blade, which can be explained as due to the coupling between lead-lag and torsion modes. Corresponding results from Hodges and Ormiston (1976) are included in Fig. 8. Comparisons show that, as before, the agreement between the two results is very good at low thrust levels and the deviation increases with the thrust.

The rotating coupled natural frequencies of the stiff-inplane blade about its steady deflected position are investigated for convergence as the number of finite elements is varied. Table 3 presents the fundamental lead-lag, flap, and torsion frequencies with increasing number of elements. It is seen that six elements are sufficient for four digit accuracy. The bandedness of the inertia and stiffness matrices is used effectively to mimimize computation time.

The solution of the flutter equations results in complex eigenvalues. The normal mode method is examined for convergence as the number of modes is varied, keeping the number of elements fixed at six. The real parts of the first three eigenvalues for different numbers of modes is given in Table 4. This table shows that five modes result in a well-converged solution (five-digit accuracy). Figure 9 shows the root locus plot of the fundamental lead-lag, flap, and torsion modes as C_T/σ is varied from 0 to 0.3. Even though blade angle-of-attack stall has been neglected, such high thrust levels are included for comparision with other theoretical results. Six finite elements and five normal modes are used in obtaining these results. The flap and torsion modes are stable over the entire range of C_T/σ considered, whereas the lead-lag mode is unstable for C_T/σ between 0.01 and 0.05 and above 0.17. The complete solution using six elements and five normal modes at a particular thrust level requires about 7 s of computation time on a CDC 7600 machine. Figure

10 shows the flutter stability boundaries as the lead-lag frequency is varied. The results of Hodges and ormiston (1976) are also shown for comparison in this figure. In this reference, the stability results are calculated using the normal mode method with five coupled rotating modes. There is general agreement between the two results. The differences that appear between the two results may be due to changes in aerodynamic forces by including all second-order terms (order ϵ^2) in the present analysis.

Figure 11 shows the root locus of the lead-lag mode of a stiff-inplane hingeless blade when the blade pitch is varied from -10 deg to 12 deg. The blade precone is zero for this case. Experimental results from Sharpe (1983) are also shown in this figure. In the theoretical analysis structural damping is included such that the results match that of the experiment at zero pitch. It is seen that the agreement between the present analysis and experiment is good at low pitch settings and not so good at higher pitch settings. Other theoretical analyses show similar discrepencies.

6.2 Articulated Blade

The same blade properties as given in Table 1 are used for the stability analysis of an articulated blade with a hinge offset of 6%. The convergence characteristics for the nonlinear steady solution, natural frequencies, and flutter eigenvalues are presented in Tables 5-7, respectively. These results confirm the conclusions reached for the hingeless blade that about eight elements and five normal modes are adequate for four-digit accuracy. As before, only a few iterations result in a converged nonlinear trim solution. The equilibrium tip deflections are plotted with respect to thrust in Fig. 12. The lead-lag tip deflections are much higher than that for the corresponding hingeless rotor blade because the lead-lag stiffness is lower when the blade is hinged. The root locus of the flutter eigenvalues obtained using six

elements and five normal modes is shown in Fig. 13. All three modes are stable over the range of C_T/σ shown.

7. MODIFICATIONS FOR ANALYSIS OF MULTIPLE-LOAD-PATH BLADES

Having shown that the finite element formulation can be successfully applied for the determination of the aeroelastic stability of single-load-path blades, the analysis is extened to include the more complex multiple-load-path blades. As indicated in the Introduction, the flexure of a bearingless blade contains one or two flexbeams and a torque tube. The analytical model of a bearingless blade is shown in Fig. 14. Each of the flexbeams and the torque tube are modelled as individual beams. For this purpose several modification have to be made to the formulation presented in the previous chapters.

7.1 Inclusion of Axial Degree of Freedom

In the analysis for single-load-path blades, the axial deflection u has been eliminated in terms of the other deflections and the expression for the centrifugal force. The force equilibrium equation in the axial direction cannot be solved a priori for multiple-load-path blades; and hence the u deflection has to be included as a degree of freedom.

7.2 Refined Finite Element

The beam element considered for discretizing multiple-load-path blades is shown in Fig. 15. This element is more refined than the simple beam element used for single-load-path blades. The element includes the axial degrees of freedom. Each element consists of two end nodes and three internal nodes with a total of fifteen degree of freedom. Each of the end nodes (1 and 2) have six degrees of freedom, namely u, v, v', w, w', and $\hat{\phi}$. There are two internal nodes for u and one internal node for $\hat{\phi}$. Two internal nodes are needed for the axial degree of freedom to accurately represent the centrifugal force distribution over the element. With

two internal nodes, the distribution of u over the element is cubic. Hence, the axial force distributiion is quadratic and of the same order as that of the centrifugal force. The internal node for the torsional deflection assures that the torque approximation over the element is of the same order as the flap and lead-lag bending moment approximations.

7.3 Displacement Compatibility Conditions at the Clevis

The element matrices are assembled, by considering displacement compatibility conditions at interelement boundaries, to form global matrices. Except at the clevis, the displacement compatibility conditions generally imply the continuity of u, v, v', w, w', and $\hat{\phi}$ across element boundaries. The root element of the outboard blade is connected to the outermost elements of the flexbeams and the torque tube through the clevis which is assumed to be rigid (Fig. 14). The inboard beams are numbered 1,2,3, etc. The displacement compatibility conditions at the clevis can be written as

$$\begin{aligned} u_i &= u - \eta_i v' \\ v_i &= v \\ v_i' &= v' \\ w_i &= w + \eta_i(\theta_{ac} + \phi) \\ w_i' &= w' \end{aligned} \tag{7.1}$$

and

$$\begin{aligned} \phi_i &= \theta_{ac} + \phi \quad (\textit{for flexbeams}) \\ \phi_i &= \phi \qquad (\textit{for torquetube}) \end{aligned} \tag{7.2}$$

where u_i, v_i, w_i, and ϕ_i are the deflections at the clevis for the ith inboard beam; and u, v, w, and ϕ are the deflections at the clevis for the outboard beam. The η_i is the elastic axis offset of the ith inboard beam from that of the outboard beam (positive forward) and θ_{ac} the difference between the collective pitch and the pretwist at the clevis (Fig. 16). Equation (7.2) for the flexbeam indicates that a rigid body pitch rotation of the outboard blade is transferred to the flexbeam as an elastic twist.

7.4 Modifications in Solution Procedure

In addition to the differences noted above, there are two major differences in the solution procedure for nonlinear trim solution. Some of the terms of the matrix $[K_0]$ depend on the centrifugal force F. The centrifugal force distribution is known a priori only over the ouboard blade; it is unknown over the flexure because of the multiple load paths involved. In obtaining the linear estimate of the steady equations, it is assumed that the centrifugal force in each of the inboard beam is in the ratio of its tensile stiffness EA. Then, at successive iterations the centrifugal force distrubution is updated using Eq. (2.6).

The lead-lag and flap stiffnesses depend on the orientation (pitch) of the cross section. The pitch distribution is known a priori for the outboard blade. For the flexbeams, the resultant pitch is the sum of the pretwist θ_{pc} and the elastic twist due to θ_{ac} at the clevis (Fig. 16). For the first iteration of the nonlinear trim solution, the pitch distribution along the flexbeams is assumed to be linear. This distribution is updated at successive iterations based on the torsional deflection.

8. APPLICATION TO MULTIPLE-LOAD-PATH BLADES

The formulation modified for multiple-load-path blades is applied to several analytical models of bearingless rotor blades in hover. The outboard blade, the flexbeams, and the torque tube are considered to be uniform. The chordwise offsets of the tension center, mass center, and aerodynamic center from the elastic axis are assumed to be zero. The section constants EB_1, EB_2, and the warping constants EC_1, EC_2 are taken to be zero. The aerodynamic forces over the flexure is neglected. A precone (β_p) of 0.05 rad (2.9 deg), Lock number (γ) of 5, and solidity ratio (σ) of 0.1 are used. The offset of the elastic axis of the flexbeams (Fig. 14) from that of the outboard blade ($\eta_1 = -\eta_3$) is taken to be $0.4c$, where c is the chord of the outboarad blade; the torque tube offset (η_2) is zero. The length of the flexure is $0.25R$. The blade structural poperties are given in Table 8; the aerodynamic properties are the same as given in Table 1. Stiff- and soft-inplane and torsionally-stiff and soft blades are considered.

8.1 Twinbeam Model with Zero Inboard Pitch

To understand the behavior of multiple-load-path blades, a simple analytical model is considered first. This model has an inboard flexure cosisting of two identical flexbeams; the torque tube is not included (Fig. 17). The pitch of the flexure is fixed at zero while the pitch of the outboard blade is varied. This is equivalent to a physical model with a pitch bearing at the clevis. First, a convergence study is made to determine the number of finite elements needed to obtain the nonlinear trim solution to a desired accuracy. Table 9 shows the steady state tip deflections $u_{0_{tip}}$, $v_{0_{tip}}$, $w_{0_{tip}}$ (nondimensionalized with respect to the rotor length), and $\hat{\phi}_{0_{tip}}$ (in rad) as the number of both the flexbeam and the outboard elements is varied. The blade considered is stiff inplane and soft in torsion. A thrust level, C_T/σ, of o.1 is used. The results show that two elements each for the flexbeams and two elements

for the outboard blade are sufficient for five digit accuracy. The nonlinear iterative solution converges rapidly since the linear solution is used as the initial estimate; only four or five iterations are needed for a converged solution.

The rotating coupled natural frequencies of the blade about its steady deflectd position are investigated for convergence as the number of finite elements is varied. Table 10 presents the fundamental lead-lag, flap, and torsion frequencies with increasing number of elements. Again, it is seen that a total of six elements, two for the outboard blade and two each for the flexbeams, are sufficient for five digit accuracy.

The solution of the flutter equations results in complex eigenvalues. The normal mode method is examined for convergence as the number of modes is varied, keeping the total number of elements fixed at six. The real parts of the first three eigenvalues for different numbers of modes is presented in Table 11. This table shows that five modes result in a converged solution (five digit accuracy).

Figure 18 shows the root locus plot of the fundamental lead-lag mode as C_T/σ is varied from 0 to 0.2. It is seen that the lead-lag mode is unstable for C_T/σ higher than about 0.05. In this figure, the results from an equivalent-beam model are also shown. In general, the properties of the equivalent-beam model are obtained by matching the fundamental frequencies of the equivalent-beam model with that of the multibeam blade. For flexbeams with uniform spanwise poperties, analytical expressions for equivalent properties can be obtained. These are given in Appendix *D*. The two results shown in Fig. 18 differ from each other, particularly at low and high levels of thrust. The results at low thrust levels are of significance to tail rotors. A careful study has been made to determine the cause of the differences between the two results. The equivalent-beam model does not accurately simulate the cross-coupling stiffness terms which are nonlinear in nature and depend on the steady deflections. Results have been computed by suppressing, in the perturbation

analysis, nonlinear cross-coupling terms of nonlinear origin from the structural stiffness matrix of the flexure, for the twin- beam as well as the equivalent beam model. These are shown in Fig. 19. Both sets of results are identical.

For the same model but considering a soft-inplane, torsionally-stiff blade, the root locus of the lead-lag mode is plotted in Fig. 20. The behaviur of this blade is very different from that of the stiff-inplane blade. The coressponding equivalent-beam model results are also included in this figure. The discrepency between the results of the two models are more pronounced, particularly at high thrust levels, than that of the stiff-inplane blade. Again the removal, in the perturbation analysis, of the cross-coupling terms of nonlinear origin from the structural stiffness matrix of the flexure makes the results identical (Fig. 21). Similar conclusions are reached from the root locus plots of the lead-lag mode of a torsionally-stiff blade (Figs. 22 and 23).

8.2 Twinbeam Model with Same Pitch For Inboard and Outboard Segments

This blade model also has a flexure consisting of two identical flexbeams; and there is no torque tube. Both the inboard and the ouboard segments are maintained at the same uniform pitch distribution. This represents a physical model with pitch bearings at the hub end of the flexbeams. The root loci of the lead-lag mode with respect to increasing level of thrust are shown in Fig. 24 for both the twinbeam and the equivalent-beam models. The results are for a stiff-inplane and torsionally-soft blade. The two results are in major disagreement with each other. This disparity is explained as follows. The fundamental frequencies of the equivalent-beam model are matched with that of the twinbeam model at a chosen pitch setting (zero in the present example). As the pitch is changed, the effective flap and lead-lag stiffnesses vary because of flap-lag coupling. This modifies the frequencies of the blade; and

the frequency match no longer exists. This phenomenon is clearlyl seen from Table 12 where the fundamental frequencies are presented for various thjrust levels. As the thrust (and hence the pitch) increases, the difference between the frequencies of the two model widens. Thus, the equivalent-beam simulation is not accurate with changing pitch. The results of Fig. 25 are for a soft-inplane blade. Again the discrepency between the twin-beam and the equivalent-beam models is big. Similar effects are observed from the results of a torsionally-stiff blade (Fig. 26).

8.3 Bearingless Model with Torque Tube

This blade has a root flexure consisting of two identical flexbeams and a torque tube in the middle. This model is a more appropriate representation of the bearingless blade. Pitch control of the blade is achieved via the torque tube by rotating the clevis. Due to the piltch application at the clevis, there is an elastic pitch distribution over the flexbeam and this is determined iteratively. As a result, the number of iterations required for convergence of the nonlinear trim solution is increased. Now it takes about ten iterations for five digit accuracy, whereas, four or five itereations have been adequate for the two previous models. The convergence characteristics are similar to the one presented for the previous models in tables 9-11. The results have indicated that a total of eight elements - two elements for the outboard blade, two for the torque tube, and two each for the flexbeams - are adequate for five digit accuracy. The root loci of the flutter eigenvalues (fundamental lead-lag, flap, and torsion modes) are shown in Fig. 27 as C_T/σ is varied from to 0.15. The flap and torsion modes are stable while the lead-lag mode becomes unstable at high levels of thrust (C_T/σ greater than about 0.13). This is a weak instability and the introduction of a small amount of structural damping would stabilize the mode.

9. GENERAL CONCLUSIONS

The finite element method has been successfully applied to determine the nonlinear trim deflections and the flutter stability of sing! ~ and multiple-load-path blades in flap bending, lead-lag bending and torsion. The formulation is based on Hamilton's principle. The spatial dependence of the equations of motion is made discrete by dividing the blade into a number of beam elements. Nonlinear trim deflections are evaluated iteratively, solving the complete set of of global equations, without making a modal transformation. The solution procedure is made efficient using the bandedness of the stiffness matrix and the linear solution as the starting vector. The coupled rotating natural modes are calculated about the trim condition of the blade. The normal mode method based on these modes is used to solve the linearized flutter equations as an eigenvalue problem.

The formulation is first applied to uniform single-load-path blades, namely hingeless and articulated. Six finite elements are sufficient to determine the trim deflections, and the free vibration characteristics. Five coupled rotating modes are adequate for the normal mode solution of the flutter equations. The steady tip deflections agree very well with that of a previous research which used modal method based on a total of fifteen nonrotating uncoupled modes; the flutter stability boundaries also show excellent agreement with that previous research based on a modal approach. The root-locus plots of flutter eigenvalues as a function of the pitch are generally in good agreement with experimental results.

Suitable modifications have been made in the formulation so as to consider multiple-load-path blades. Numerical results are presented for several baringless models. Results of the redundantbeam analysis are compared with that of the equivalent-beam modelling; and the following important conclusions are reached. The equivalent beam does not simulate the nonlinear structural coupling terms ap-

propriately. Also, the properties of the equivalent beam are estimated by matching frequencies with the bearingless blade at a particular pitch setting. At other pitch settings, the frequencies change and the match no longer holds. As a result, the stability results obtained using the equivalent-beam model are inaccurate.

Future extensions may include forward flight, ground and air resonance, and consideration of composite blades.

APPENDIX A. NONDIMENSIONAL QUANTITIES

The nondimensional quantities in δU, δT, and δW [Eqs. (2.17), (2.18), and (2.19)] are defined here. These symbols are retained after nondimensionalisation.

Old quantity	New quantity	Assumed order of magnitude
x/R	x	1
$(\dot{})/\Omega$	$\dot{()}$	1
v/R	v	ϵ
w/R	w	ϵ
ϕ	ϕ	ϵ
θ	θ	1
$F/m_0\Omega^2R^2$	F	1
$EI_y/m_0\Omega^2R^4$	EI_y	1
$EI_z/m_0\Omega^2R^4$	EI_z	1
$GJ/m_0\Omega^2R^4$	GJ	1
$EA/m_0\Omega^2R^2$	EA	$1/\epsilon^2$
$EB_1/m_0\Omega^2R^3$	EB_1	ϵ^2
$EB_2/m_0\Omega^2R^3$	EB_2	ϵ
$EC_1/m_0\Omega^2R^3$	EC_1	ϵ^2
$EC_2/m_0\Omega^2R^3$	EC_2	ϵ
k_A/R	k_A	ϵ
k_{m_1}/R	k_{m_1}	ϵ
k_{m_2}/R	k_{m_2}	ϵ
e_a/R	e_a	$\epsilon^{3/2}$
e_θ/R	e_θ	$\epsilon^{3/2}$
β_p	β_p	ϵ

APPENDIX B. STEADY-STATE ELEMENT MATRICES

The expressions for steady-state element stiffness matrix and load vector are derived from the steady part of Eq. (4.2).

$$\Delta_{0_i} \equiv \delta U_{0_i} - \delta T_{0_i} - \delta W_{0_i} \tag{B.1}$$

The strain energy, kinetic evergy, and the virtual work contributions of the ith element in steady state are obtained from Eqs. (2.17), (2.18), and (2.19) by dropping all time dependent terms and writing

$$\begin{aligned} \sin\left(\theta + \hat{\phi}\right) &\approx \sin\theta + \hat{\phi}\cos\theta \\ \cos\left(\theta + \hat{\phi}\right) &\approx \cos\theta - \hat{\phi}\sin\theta \end{aligned} \tag{B.2}$$

This results in

$$
\begin{aligned}
\frac{\delta U_{0_i}}{m_0\Omega^2R^3} = \int_0^{l_i} \Big\langle & F_0\Big(v_0'\delta v' + w_0'\delta w'\Big) \\
& + GJ\Big(\hat{\phi}_0'\delta\hat{\phi}' + \hat{\phi}_0'w_0'\delta v'' + \hat{\phi}_0'v_0''\delta w' + v_0''w_0'\delta\hat{\phi}'\Big) \\
& + \Big[F_0k_A^2\Big(\theta' + \underline{\hat{\phi}_0'}\Big) - \underline{\underline{EAk_A^4\theta'^2\phi_0' + EAe_ak_A^2\theta'(v_0''\cos\theta + w_0''\sin\theta)}} \\
& + \underline{\underline{EB_1\theta'^2\hat{\phi}_0'}} - EB_2\theta'(v_0''\cos\theta + w_0''\sin\theta)\Big]\delta\hat{\phi}' \\
& + \Big[\underline{\underline{EC_1\hat{\phi}_0''}} + EC_2(w_0''\cos\theta - v_0''\sin\theta)\Big]\delta\hat{\phi}'' \\
& + \Big[-F_0e_a\cos\theta + \Big(EI_z\cos^2\theta + EI_y\sin^2\theta\Big)v_0'' \\
& + (EI_z - EI_y)\hat{\phi}_0(w_0''\cos 2\theta - v_0''\sin 2\theta) \\
& + \frac{1}{2}(EI_z - EI_y)w_0''\sin 2\theta - EAe_a^2\Big(v_0''\cos^2\theta + \frac{1}{2}w_0''\sin 2\theta\Big) \\
& + \Big(EAe_ak_A^2 - EB^2\Big)\theta'\hat{\phi}_0'\cos\theta - EC_2\hat{\phi}_0''\sin\theta\Big]\delta v'' \\
& + \Big[-F_0e_a\sin\theta + \Big(EI_z\sin^2\theta + EI_y\cos^2\theta\Big)w_0'' \\
& + (EI_z - EI_y)\hat{\phi}_0(v_0''\cos 2\theta + w_0''\sin 2\theta) \\
& + \frac{1}{2}(EI_z - EI_y)v_0''\sin 2\theta - EAe_a^2\Big(w_0''\sin^2\theta + \frac{1}{2}v_0''\sin 2\theta\Big) \\
& + \Big(EAe_ak_A^2 - Eb^2\Big)\theta'\hat{\phi}_0'\sin\theta - EC_2\hat{\phi}_0''\cos\theta\Big]\delta w'' \\
& + \Big[F_0e_a\Big(v_0''\sin\theta - w_0''\cos\theta\Big) \\
& + \underline{(EI_z - EI_y)\Big\{\frac{1}{2}\Big(w_0''^2 - v_0''^2\Big)\sin 2\theta + v_0''w_0''\cos 2\theta\Big\}}\Big]\delta\hat{\phi}\Big\rangle dx_i \qquad (B.3)
\end{aligned}
$$

$$\frac{\delta T_{0_i}}{m_0\Omega^2R^3} = \int_0^{l_i} m\Big\{\Big[v_0 + e_g\Big(\cos\theta - \hat{\phi}_0\sin\theta\Big)\Big]\delta v$$
$$- \beta_p x\delta w$$
$$- \Big[\frac{1}{2}\Big(k_{m2}^2 - k_{m1}^2\Big)\Big(\frac{1}{2}\sin 2\theta\hat{\phi}_0\cos 2\theta\Big) + e_g x(w_0'\cos\theta - v_0'\sin\theta)$$
$$+ e_g v_0\sin\theta + e_g\beta_p x\cos\theta\Big]\delta\hat{\phi}$$
$$- e_g x\Big(\cos\theta - \hat{\phi}_0\sin\theta\Big)\delta v'$$
$$- e_g x\Big(x\sin\theta + \hat{\phi}_0\cos\theta\Big)\delta w'\Big\}\,dx_i \qquad (B.4)$$

and

$$\frac{\delta W_{0_i}}{m_0\Omega^2R^3} = \int_0^{l_i}\Big(L_{v_0}\delta v + L_{w_0}\delta w + M_{\phi_0}\delta\psi\Big)\,dx_i \qquad (B.5)$$

where the steady-state aerodynamic forces are

$$
\begin{aligned}
L_{v_0} = \frac{\gamma}{6}\Big\langle & \cos\theta\Big\{-d_0x^2\cos^2\theta + (c_0-d_1)\Big(-\frac{1}{2}x^2\sin 2\theta + x\lambda_i cos2\theta\Big) \\
& + (c_1-d_2)\Big[(x\sin\theta-\lambda_i\cos\theta)^2 - 2x\eta_r\beta_p\sin\theta\Big]\Big\} \\
& + \sin\theta\Big\{c_0\Big(x^2\cos^2\theta + x\lambda_i sin2\theta\Big) \\
& + (c_1+d_0)\Big[x\cos\theta(-x\sin\theta+\lambda_i\cos\theta+\eta_r\beta_p) - x\lambda_i\sin^2\theta + \frac{1}{2}\lambda_i^2\sin 2\theta\Big] \\
& + d_1\Big(x^2\sin^2\theta - x\lambda_i\sin 2\theta\Big)\Big\} \\
& - u_0x(d_0+d_2)\sin 2\theta\sin\theta \\
& - v_0x\beta_p[(c_1-d_2)\sin 2\theta\cos\theta + (c_1+d_0)\sin\theta\cos 2\theta] \\
& + w_0x\beta_p(d_0+d_2)\sin 2\theta\sin\theta \\
& + w_0'2x\eta_r(-c_1+d_0+2d_2)\sin\theta\cos\theta \\
& + \hat{\phi}_0\Big(\cos\theta\Big[-(c_0-d_1)x^2\cos 2\theta + (c_1-d_2)\Big(x^2\sin 2\theta - 2x\lambda_i\cos 2\theta\Big)\Big] \\
& - \sin\theta\Big[(c_0-d_1)x^2\sin 2\theta + (c_1+d_0)\Big(x^2\cos 2\theta + 2x\lambda_i\sin 2\theta\Big)\Big] \\
& - \sin\theta\Big\{-d_0x^2\cos^2\theta + (c_0-d_1)\Big(-\frac{1}{2}x^2\sin 2\theta + x\lambda_i cos2\theta\Big) \\
& + (c_1-d_2)\Big[(x\sin\theta-\lambda_i\cos\theta)^2 - 2x\eta_r\beta_p\sin\theta\Big]\Big\} \\
& + \cos\theta\Big\{c_0\Big(x^2\cos^2\theta + x\lambda_i sin2\theta\Big) \\
& + (c_1+d_0)\Big[x\cos\theta(-x\sin\theta+\lambda_i\cos\theta+\eta_r\beta_p) - x\lambda_i\sin^2\theta + \frac{1}{2}\lambda_i^2\sin 2\theta\Big] \\
& + d_1\Big(x^2\sin^2\theta - x\lambda_i\sin 2\theta\Big)\Big\}\Big) \\
& \underline{- v_0v_0'x(d_0+d_2)\sin\theta\sin 2\theta} \\
& \underline{- v_0w_0'x[-(c_1-d_2)\sin 2\theta\cos\theta + (c_1+d_0)\sin\theta\cos 2\theta]} \\
& \underline{- v_0'^2x^2\frac{3}{2}(d_0+d_2)\sin^2\theta\cos\theta} \\
& \underline{- v_0'w_0'x^2\Big[(c_1-d_2)\Big(\sin 2\theta\cos\theta - \sin^3\theta\Big)} \\
& \underline{+ (c_1+d_0)\Big(-\sin 2\theta\cos\theta + \sin^3\theta\Big)\Big]}\Big\rangle
\end{aligned}
\qquad (B.6)
$$

$$
\begin{aligned}
L_{w_0} = \frac{\gamma}{6}\Big\langle & \sin\theta\Big\{-d_0x^2\cos^2\theta+(c_0-d_1)\Big(-\frac{1}{2}x^2\sin 2\theta+x\lambda_i cos2\theta\Big)\\
& +(c_1-d_2)\Big[(x\sin\theta-\lambda_i\cos\theta)^2-2x\eta_r\beta_p\sin\theta\Big]\Big\}\\
& -\cos\theta\Big\{c_0\Big(x^2\cos^2\theta+x\lambda_i sin2\theta\Big)\\
& +(c_1+d_0)\Big[x\cos\theta(-x\sin\theta+\lambda_i\cos\theta+\eta_r\beta_p)-x\lambda_i\sin^2\theta+\frac{1}{2}\lambda_i^2\sin 2\theta\Big]\\
& +d_1\Big(x^2\sin^2\theta-x\lambda_i\sin 2\theta\Big)\Big\}\\
& -u_0\,2x\Big[(c_1-d_2)\sin^3\theta+(c_1+d_0)\sin\theta\cos^2\theta\Big]\\
& -v_0x\beta_p[(c_1-d_2)\sin\theta\sin 2\theta+(c_1+d_0)\cos\theta\cos 2\theta]\\
& -w_0\,2x\beta_p\Big[(c_1-d_2)\sin^3\theta+(c_1+d_0)\sin\theta\cos^2\theta\Big]\\
& -w_0'2x\eta_r\Big[2(c_1-d_2)\sin^2\theta+(c_1+d_0)\cos^2\theta\Big]\\
& +\hat{\phi}_0\Big(\sin\theta\Big[-(c_0-d_1)x^2\cos 2\theta+(c_1+d_0)\Big(x^2\sin 2\theta-2x\lambda_i\cos 2\theta\Big)\Big]\\
& +\cos\theta\Big[(c_0-d_1)x^2\sin 2\theta(c_1+d_0)\Big(x^2\cos 2\theta+2x\lambda_i\sin 2\theta\Big)\Big]\\
& +\cos\theta\Big\{-d_0x^2\cos^2\theta+(c_0-d_1)\Big(-\frac{1}{2}x^2\sin 2\theta+x\lambda_i cos2\theta\Big)\\
& +(c_1-d_2)\Big[(x\sin\theta-\lambda_i\cos\theta)^2-2x\eta_r\beta_p\sin\theta\Big]\Big\}\\
& +\sin\theta\Big\{c_0\Big(x^2\cos^2\theta+x\lambda_i sin2\theta\Big)\\
& +(c_1+d_0)\Big[x\cos\theta(-x\sin\theta+\lambda_i\cos\theta+\eta_r\beta_p)-x\lambda_i\sin^2\theta+\frac{1}{2}\lambda_i^2\sin 2\theta\Big]\\
& +d_1\Big(x^2\sin^2\theta-x\lambda_i\sin 2\theta\Big)\Big\}\Big)\\
& -v_0v_0'x\Big[2(c_1-d_2)\sin^3\theta+(c_1+d_0)\sin 2\theta\cos\theta\Big]\\
& -v_0w_0'x[(c_1-d_2)\sin\theta\sin 2\theta+(c_1+d_0)\cos\theta\cos 2\theta]\\
& -v_0'^2x^2\Big[(c_1-d_2)\sin^3\theta+(c_1+d_0)\sin\theta\cos^2\theta\Big]\\
& +v_0'w_0'x^2[(c_1-d_2)\sin\theta\sin 2\theta+(c_1+d_0)\cos\theta\cos 2\theta]\\
& -w_0'^2x^2\frac{1}{2}\Big[(c_1-d_2)\sin^3\theta+(c_1+d_0)\sin\theta\cos^2\theta\Big]\Big\rangle
\end{aligned}
\qquad (B.7)
$$

$$M_{\phi_0} = \frac{\gamma}{6} x^2 \left\{ cC_{Mac} - e_d \left[(c_1 + d_0) \sin\theta \cos\theta - d_1 \sin^2\theta \right] \right\} \tag{B.8}$$

The Δ_{0_i} of Eq. (B.1) can also be written as

$$\Delta_{0_i} = \{\delta q_i\}[K_i]_0\{q_i\}_0 + \{\delta q_i\}\{Q_i\}_0 \tag{B.9}$$

By comparing Eqs. (B.1) and (B.9) the element stiffness matrix and the load vector can be written. The contribution from δU_{0_i} and δT_{0_i} to the element stiffenss matrix and the load vector is given as follows (the contribution from δW_{0_i} can be easily inferred from L_{v_0}, L_{w_0}, and M_{ϕ_0}).

$$[K_i]_0 = \begin{bmatrix} [K_{vv}] & [K_{vw}] & [K_{v\phi}] \\ [K_{wv}] & [K_{ww}] & [K_{w\phi}] \\ [K_{\phi v}] & [K_{\phi w}] & [K_{\phi\phi}] \end{bmatrix} \tag{B.10}$$

and

$$\{Q_i\}_0 = \begin{Bmatrix} \{Q_v\} \\ \{Q_w\} \\ \{Q_\phi\} \end{Bmatrix} \tag{B.11}$$

where

$$[K_{vv}] = \int_0^{l_i} \Big[F_0 \{H'\}\{H'\}^T + \left(EI_z \cos^2\theta + EI_y \sin^2\theta - EAe_a^2 \cos\theta^2 \right) \{H''\}\{H''\}^T - m\{H\}\{H\}^T \Big] dx_i$$

$$[K_{vw}] = \int_0^{l_i} \frac{1}{2} \left(EI_z - EI_y - EAe_a^2 \right) \sin 2\theta \{H''\}\{H''\}^T dx_i$$

$$
\begin{aligned}
[K_{v\phi}] = \int_0^{l_i} \Big[& \Big(EAe_a k_A^2 - EB_2\Big)\theta' \cos\theta \{H''\}\Big\{H'_\phi\Big\}^T \\
& + F_0 e_a \sin\theta \{H''\}\{H_\phi\}^T \\
& - EC_2 \sin\theta \{H''\}\Big\{H''_\phi\Big\}^T \\
& + me_g \sin\theta \{H\}\{H_\phi\}^T \\
& - me_g x \sin\theta \{H'\}\{H_\phi\}^T \\
& - (EI_z - EI_y)\sin 2\theta \{H''\}\{H''\}^T \{v_0^*\}\{H_\phi\}^T \\
& + (EI_z - EI_y)\cos 2\theta \{H''\}\{H''\}^T \{w_0^*\}\{H_\phi\}^T \\
& + GJ\{H''\}\{H'\}^T \{w_0^*\}\Big\{H'_\phi\Big\}^T \Big] dx_i
\end{aligned}
$$

$$
[K_{wv}] = [K_{vw}]
$$

$$
[K_{ww}] = \int_0^{l_i} \Big[F_0 \{H'\}\{H'\}^T + \Big(EI_z \sin^2\theta + EI_y \cos^2\theta - EAe_a^2 \sin^2\theta\Big)\{H''\}\{H''\}^T \Big] dx_i
$$

$$
\begin{aligned}
[K_{w\phi}] = \int_0^{l_i} \Big[& \Big(EAe_a k_A^2 - EB_2\Big)\theta' \sin\theta \{H''\}\Big\{H'_\phi\Big\}^T \\
& - F_0 e_a \cos\theta \{H''\}\{H_\phi\}^T \\
& + EC_2 \cos\theta \{H''\}\Big\{H''_\phi\Big\}^T \\
& + me_g x \cos\theta \{H'\}\{H_\phi\}^T \\
& + (EI_z - EI_y)\cos 2\theta \{H''\}\{H''\}^T \{v_0^*\}\{H_\phi\}^T \\
& + (EI_z - EI_y)\sin 2\theta \{H''\}\{H''\}^T \{w_0^*\}\{H_\phi\}^T \\
& + GJ\{H'\}\{H''\}^T \{v_0^*\}\Big\{H'_\phi\Big\}^T \Big] dx_i
\end{aligned}
$$

$$[K_{\phi v}] = \int_0^{l_i} \Big[\Big(EAe_a k_A^2 - EB_2 \Big) \theta' \cos\theta \Big\{ H'_\phi \Big\} \{H''\}^T$$
$$+ F_0 e_a \sin\theta \{H_\phi\} \{H''\}^T$$
$$- EC_2 \sin\theta \Big\{ H''_\phi \Big\} \{H''\}^T$$
$$+ me_g \sin\theta \{H_\phi\} \{H\}^T$$
$$- me_g x \sin\theta \{H_\phi\} \{H'\}^T$$
$$- \frac{1}{2} (EI_z - EI_y) \sin 2\theta \{H_\phi\} \{v_0^*\}^T \{H''\} \{H''\}^T$$
$$+ (EI_z - EI_y) \cos 2\theta \{H_\phi\} \{w_0^*\}^T \{H''\} \{H''\}^T \Big] dx_i$$

$$[K_{\phi w}] = \int_0^{l_i} \Big[\Big(EAe_a k_A^2 - EB_2 \Big) \theta' \sin\theta \Big\{ H'_\phi \Big\} \{H''\}^T$$
$$- F_0 e_a \cos\theta \{H_\phi\} \{H''\}^T$$
$$+ EC_2 \cos\theta \Big\{ H''_\phi \Big\} \{H''\}^T$$
$$+ me_g x \cos\theta \{H_\phi\} \{H'\}^T$$
$$- \frac{1}{2} (EI_z - EI_y) \sin 2\theta \{H_\phi\} \{w_0^*\}^T \{H''\} \{H''\}^T$$
$$+ GJ \Big\{ H'_\phi \Big\} \{v_0^*\}^T \{H''\} \{H'\}^T \Big] dx_i$$

$$[K_{\phi\phi}] = \int_0^{l_i} \Big[\Big(GJ + F_0 k_A^2 - EAk_A^4 \theta'^2 + EB_1 \theta'^2 \Big) \Big\{ H'_\phi \Big\} \Big\{ H'_\phi \Big\}^T$$
$$+ EC_1 \Big\{ H''_\phi \Big\} \Big\{ H''_\phi \Big\}^T$$
$$+ m \Big(k_{m_2}^2 - k_{m_1}^2 \Big) \cos 2\theta \{H_\phi\} \{H_\phi\}^T \Big] dx_i$$

$$\{Q_v\} = \int_0^{l_i} \left[F_0 e_a \cos\theta \{H''\} + me_g \cos\theta \{H\} - me_g x \cos\theta \{H'\} \right] dx_i$$

$$\{Q_w\} = \int_0^{l_i} \left[F_0 e_a \sin\theta \{H''\} + m\beta_p x \{H\} - me_g x \sin\theta \{H'\} \right] dx_i$$

$$\{Q_\phi\} = \int_0^{l_i} \Big[-F_0 k_A^2 \theta' \Big\{ H'_\phi \Big\} - \frac{1}{2} m \Big(k_{m_2}^2 - k_{m_1}^2 \Big) \sin 2\theta \{H_\phi\} - me_g \beta_p x \cos\theta \{H_\phi\} \Big] dx_i$$

The column vectors $\{H\}$, $\{H_\phi\}$, and $\{v_0^*\}$ are defined as

$$\{H\}^T = \lfloor H_1 \quad H_2 \quad H_3 \quad H_4 \rfloor$$

$$\{H_\phi\}^T = \lfloor H_{\phi_1} \quad H_{\phi_2} \rfloor$$

$$\{v_0^*\}^T = \lfloor v_{0_1} \quad v'_{0_1} \quad v_{0_2} \quad v'_{0_2} \rfloor$$

A similar definition holds good for $\{w_0^*\}$.

APPENDIX C. PERTURBATION ELEMENT MATRICES

The strain and kinetic energy contributions to the perturbation inertia, damping, and stiffness element matrices are given here. The contribution of the aerodynamic forces is easily inferred from Eqs.(3.16)-(3.18). Since these matrices are linearized about the steady deflection, the inertia and stiffness matrices are symmetric whereas the damping matrix is antisymmetric; but the nonconservative aerodynamic terms will make the damping and stiffness matrices asymmetric.

Inertia Matrix

The element inertia matrix for the ith element is written as

$$[M_i] = \begin{bmatrix} [M_{vv}] & [M_{vw}] & [M_{v\phi}] \\ [M_{wv}] & [M_{ww}] & [M_{w\phi}] \\ [M_{\phi v}] & [M_{\phi w}] & [M_{\phi\phi}] \end{bmatrix} \qquad (C.1)$$

where

$$[M_{vv}] = \int_0^{l_i} m\{H\}\{H\}^T dx_i$$

$$[M_{vw}] = [0]$$

$$[M_{v\phi}] = -\int_0^{l_i} me_g \sin\theta_0 \{H\}\{H\}^T dx_i$$

$$[M_{ww}] = \int_0^{l_i} m\{H\}\{H\}^T dx_i$$

$$[M_{w\phi}] = \int_0^{l_i} me_g \cos\theta_0 \{H\}\{H\}^T dx_i$$

$$[M_{\phi\phi}] = \int_0^{l_i} mk_m^2 \{H\}\{H\}^T dx_i$$

Damping Matrix

The element damping matrix for the ith element is written as

$$[C_i] = \begin{bmatrix} [C_{vv}] & [C_{vw}] & [C_{v\phi}] \\ [C_{wv}] & [C_{ww}] & [C_{w\phi}] \\ [C_{\phi v}] & [C_{\phi w}] & [C_{\phi\phi}] \end{bmatrix} \qquad (C.2)$$

where

$$[C_{vv}] = \int_0^{l_i} 2me_g \cos\theta_0 \left[\{H'\}\{H\}^T - \{H\}\{H'\}^T\right] dx_i$$

$$[C_{vw}] = \left[-2m\beta_p \{H\}\{H\}^T - 2me_g \sin\theta_0 - \{H\}\{H'\}^T\right] dx_i$$

$$[C_{v\phi}] = [0]$$

$$[C_{ww}] = [0]$$

$$[C_{w\phi}] = [0]$$

$$[C_{\phi\phi}] = [0]$$

Stiffness Matrix

$$[K_i] = \begin{bmatrix} [K_{vv}] & [K_{vw}] & [K_{v\phi}] \\ [K_{wv}] & [K_{ww}] & [K_{w\phi}] \\ [K_{\phi v}] & [K_{\phi w}] & [K_{\phi\phi}] \end{bmatrix} \qquad (C.3)$$

where

$$[K_{vv}] = \int_0^{l_i} \Big[F_0 \{H'\}\{H'\}^T + \Big(EI_z \cos^2\theta_0 + EI_y \sin^2\theta_0 - EAe_a^2 \cos\theta_0^2 \Big) \{H''\}\{H''\}^T - m\{H\}\{H\}^T \Big] dx_i$$

$$[K_{vw}] = \int_0^{l_i} \Big[\frac{1}{2} \Big(EI_z - EI_y - EAe_a^2 \Big) \sin 2\theta_0 \{H''\}\{H''\}^T + GJ\{H''\} \Big\{ H'_\phi \Big\}^T \Big\{ \hat{\phi}_0^* \Big\} \{H'\}^T \Big] dx_i$$

$$
\begin{aligned}
[K_{v\phi}] = \int_0^{l_i} \Big[& \left(EAe_a k_A^2 - EB_2\right)\theta_0' \cos\theta_0 \{H''\}\left\{H_\phi'\right\}^T \\
& + F_0 e_a \sin\theta_0 \{H''\}\{H_\phi\}^T \\
& - EC_2 \sin\theta_0 \{H''\}\left\{H_\phi''\right\}^T \\
& + me_g \sin\theta_0 \{H\}\{H_\phi\}^T \\
& - me_g x \sin\theta_0 \{H'\}\{H_\phi\}^T \\
& - (EI_z - EI_y)\sin 2\theta_0 \{H''\}\{H''\}^T \{v_0^*\}\{H_\phi\}^T \\
& + (EI_z - EI_y)\cos 2\theta_0 \{H''\}\{H''\}^T \{w_0^*\}\{H_\phi\}^T \\
& + GJ\{H''\}\{H'\}^T \{w_0^*\}\left\{H_\phi'\right\}^T \Big] dx_i
\end{aligned}
$$

$$
\begin{aligned}
[K_{w\phi}] = \int_0^{l_i} \Big[& \left(EAe_a k_A^2 - EB_2\right)\theta_0' \sin\theta_0 \{H''\}\left\{H_\phi'\right\}^T \\
& - F_0 e_a \cos\theta_0 \{H''\}\{H_\phi\}^T \\
& + EC_2 \cos\theta_0 \{H''\}\left\{H_\phi''\right\}^T \\
& + me_g x \cos\theta_0 \{H'\}\{H_\phi\}^T \\
& + (EI_z - EI_y)\cos 2\theta_0 \{H''\}\{H''\}^T \{v_0^*\}\{H_\phi\}^T \\
& + (EI_z - EI_y)\sin 2\theta_0 \{H''\}\{H''\}^T \{w_0^*\}\{H_\phi\}^T \\
& + GJ\{H'\}\{H''\}^T \{v_0^*\}\left\{H_\phi'\right\}^T \Big] dx_i
\end{aligned}
$$

$$
\begin{aligned}
[K_{\phi\phi}] = \int_0^{l_i} \Big[& \left(GJ + F_0 k_A^2 - EAk_A^4 \theta_0^2 + EB_1 \theta_0'^2\right)\left\{H_\phi'\right\}\left\{H_\phi'\right\}^T \\
& + EC_1 \left\{H_\phi''\right\}\left\{H_\phi''\right\}^T \\
& + m\left(k_{m_2}^2 - k_{m_1}^2\right)\cos 2\theta_0 \{H_\phi\}\{H_\phi\}^T \Big] dx_i
\end{aligned}
$$

The column vectors $\{H\}$, $\{H_\phi\}$, and $\{v_0^*\}$ are defined as

$$\{H\}^T = \lfloor H_1 \quad H_2 \quad H_3 \quad H_4 \rfloor$$

$$\{H\phi\}^T = \lfloor H_{\phi_1} \quad H_{\phi_2} \rfloor$$

$$\{v_0^*\}^T = \lfloor v_{0_1} \quad v'_{0_1} \quad v_{0_2} \quad v'_{0_2} \rfloor$$

A similar definition holds good for $\{w_0^*\}$ and $\left\{\hat{\phi}_0^*\right\}$. Also θ_0 is defined as

$$\theta_0 = \theta + \hat{\phi}_0$$

APPENDIX D. EQUIVALENT-BEAM PROPERTIES

Mathematical expressions of equivalent properties for modelling twin beams (Fig. 17) as an equivalent beam are presented here.

$$
\begin{aligned}
(EA)_e &= (EA)_1 + (EA)_2 \\
(EI_y)_e &= (EI_y)_1 + (EI_y)_2 \\
(EI_z)_e &\approx (EI_z)_1 + (EI_z)_2 + \eta_1^2(EA)_1 + \eta_2^2(EA)_2 \\
(GJ)_e &= (GJ)_1 + (GJ)_2 + 12\frac{(\eta_1 - \eta_2)^2}{L_f^2}\frac{(EI_y)_1(EI_y)_2}{(EI_y)_1 + (EI_y)_2} \\
\left(Ak_A^2\right)_e &= \left(Ak_A^2\right)_1 + \left(Ak_A^2\right)_2 + \eta_1^2 A_1 + \eta_2^2 A_2 \\
\left(mk_m^2\right)_e &= \left(mk_m^2\right)_1 + \left(mk_m^2\right)_2 + \eta_1^2 m_1 + \eta_2^2 m_2 \\
m_e &= m_1 + m_2
\end{aligned}
$$

The subscripts e,1, and 2 refer, respectively, to the equivalent beam, flexbeam one, and flexbeam two; and L_f is the length of the flexure. These expressions become simpler for the present case where the two beams are identical.

REFERENCES

Bielawa, R.L., "Aeroelastic Characteristics of Composite Bearingless Blades," 32nd Annual Forum of the American Helicopter Society, Paper no. 1032, May 1976.

Brown, K.M. and Dennis, J.E., "Derivative Free Analogues of the Levenberg-Marquardt and Gauss Algorithms for Nonlinear Least Squares Approximations," *Numerische Mathematik*, 18, 1972, pp. 289–297.

Chopra, I. and Dugundji, J., "Nonlinear Dynamic Response of a Wind Turbine Blade," *Journal of Sound and Vibration*, Vol. 63(2), 1979, pp. 265–286.

Dixon, P.G.C. and Bishop, H.E., "The Bearingless Main Rotor," *Journal of the American Helicopter Society*, Vol. 25, July 1980, pp. 15–21.

Friedmann, P. and Tong, P., "Nonlinear Flap-Lag Dynamics of Hingeless Helicopter Blades in Hover and Forward Flight," *Journal of Sound and Vibration*, Vol. 30(1), 1973, pp.9–31.

Fridemann, P. and Straub, F.K., "Application of the Finite Element Method to Rotary Wing Aeroelasticity," *Journal of the American Helicopter Society*, Vol.25, Jan. 1980, pp. 36–44.

Fung, Y.C., *An Introduction to the Theory of Aeroelasticity*, Dover Publications, Inc., New York, 1969.

Gallagher, R.H., *Finite Element Analysis Fundamentals*, Prentice Hall, Inc., Englewood Cliffs, New Jersey, 1975.

Harvey, K.W., "Aeroelastic Analysis of a Bearingless Rotor," American Helicopter Society Mideast Region Symposium on Rotor Technology, Aug. 1976.

Hodges, D.H. and Dowell, E.H., "Nonlinear Equations of Motion for the Elastic Bending and Torsion of Twisted Nonuniform Blades," NASA TN D-7818, Dec. 1974.

Hodges, D.H. and Ormiston, R.A. "Stability of Elastic Bending and Torsion of Uniform Cantilever Rotor Blades in Hover with Variable Structural Coupling," NASA TN D-8192, Apr. 1976.

Hodges, D.H., "An Aeromechanical Stability Analysis for Bearingless Rotor Helicopters," *Journal of American Helicopter Society*, Vol. 24, Jan. 1979, pp. 2–9.

Hodges, D.H., Ormiston, R.A., and Peters, D.A., "On the Nonlinear Deformation Geometry of Euler-Bernoulli Beams," NASA TP 1566, Apr. 1980.

Hodges, D.H. and Rutkowski, M.J., "Free-Vibration Analysis of Rotating Beams by a Variable-Order Finite-Element Method," *AIAA Journal*, Vol. 19, Nov. 1981, pp. 1459-1466.

Houbolt, J.C. and Brooks, G.W., "Differential Equations of Motion for Combined Flapwise Bending, Chorwise Bending, and Torsion of Twisted, Nonuniform Rotor Blades," NACA Rep. 1346, 1958.

Johnson, W., "Flap-Lag-Torsion Dynamics of a Uniform, Cantilever Rotor Blade in Hover," NASA TM 73248, May 1977.

Jones, J.P., "The Influence of the Wake on the Flutter and Vibration of Rotor Blades," *Aeronautical Quarterly*, Vol. IX, 1958, 258–286.

Jones, W.P. and Rao, B.M., "Compressibility Effects on Oscillating Rotor Blades in Hovering Flight," *AIAA Journal*, Vol. 8, Feb. 1970, pp. 321–329.

Jones, W.P. and Rao, B.M., "Tip Vortex Effects on Oscillating Rotor Blades in Hovering Flight," *AIAA Journal*, Vol. 9, Jan. 1971, pp. 106–113.

Kato, K. and Yamane, T., "A Calculation of Rotor Impedance for Hovering Articulated-Rotor Helicopters," *Journal of Aircraft*, Vol. 16, Jan. 1979, pp. 15–22.

Kato, K. and Yamane, T., "Calculation of Rotor Impedance for Articulated-Rotor Helicopters in Forward Flight," *Journal of Aircraft*, Vol. 16, July 1979, pp. 470–476.

Kato, K. and Yamane, T., "Experimental Substantiation for Hovering Rotor Vertical Impedance Calculations," *Journal of Aircraft*, Vol. 18, June 1981, pp. 445–450.

Kaza, K.R.V. and Kvaternik, R.G., "A Critical Examination of The Flap-Lag Dynamics of Helicopter Rotor Blades in Hover and Forward Flight," 32nd Annual Forum of the American Helicopter Society, Paper No. 1034, May 1976.

Kvaternik, R.G. and Kaza, K.R.V., "Nonlinear Curvature Expressions for Combined Flapwise Bending, Chordwise Bending, Torsion, and Extension of Twisted Rotor Blades," NASA TM X-73, 997, 1976.

Loewy, R.G., "A Two-Dimensional Approximation to the Unsteady Aerodynamics of Rotary Wings," *Journal of the Aeronautical Sciences*, Vol. 24, Feb. 1957, pp. 81–92.

Murthy, V.R. and Pierce, G.A., "Effect of Phase Angle on Multibladed Rotor Flutter," *Journal of Sound and Vibration*, Vol. 48, No. 2, 1976, pp. 221–234.

Murty, A.V.K. and Raman, A., "Nonlinear Dynamic Analysis of Rotors by Finite Element Method," *Journal of Sound and Vibration*, Vol. 69, No. 4, 1980, pp. 559–568.

Nagaraj.V.T. and Shanthakumar P., "Rotor Blade Vibrations by the Galerkin Finite Element Method," *Journal of Sound and Vibration*, Vol. 43, No. 3, 1975, pp. 575–577.

Ormistion, R.A. and Hodges, D.H., "Linear Flap-Lag Dynamics of Hingeless Helicopter Rotor Blades in Hover," *Journal of the American Helicopter Society*, Vol. 17, Apr. 1972, pp. 2–14.

Peters, D.A. and Gaonkar, G.H., "Theoretical Flap-Lag Damping With Various dynamic Inflow Models," *Journal of the American Helicopter Society*, Vol. 25, July 1980, pp. 29–36.

Putter, S. and Manor, H., "Natural Frequencies of Radial Rotating Beams," *Journal of Sound and Vibration*, Vol. 56, No.2, 1978, pp. 175–185.

Rosen, A. and Friedmann, P., "Nonlinear Equations of Equilibrium for Elastic Hellicopter or Wind Turbine Blades Undergoing Moderate Deformations," NASA CR-159478, Dec. 1978.

Sharpe, D.L., "An Experimental Investigation of the Flap-Lag-Torsion Aeroelastic Stability of a Small-Scale Hingeless Helicopter Rotor in Hover," NASA TP (to be published in 1983).

Straub, F.K. and Friedmann, P.P., "A Galerkin Type Finite Element for Rotary-Wing Aeroelasticity in Hover and Forward Flight," Vertica, Vol. 5, 1981, pp. 75–98.

Timman, R. and Van de Vorren, A.I., "Flutter of a Helicopter Rotor Rotating in Its Own Wake," *Journal of the Aeronautical Sciences*, Vol. 24, Sep. 1957, pp. 694–702.

Warmbrodt, W. and McCloud III, J.L., "A Full-Scale Wind Tunnel Investigation of a Helicopter Bearingless Main Rotor," NASA TM 81321, Aug. 1981.

Yasue, M., "Gust Response and Its Alleviation for a Hingeless Helicopter Rotor in Cruising Flight," ASRL-TR-189-1, Dept. of Aeronautics, Massachusetts Institute of Technology, Cambridge, Mass., Sep. 1978.

Table 1. Values of parameters of uniform blade for numerical results

Parameter	Numerical Value
$EI_y/m\Omega^2R^4$	0.014486 ($\omega_w = 1.15$)
$EI_z/m\Omega^2R^4$	0.026655 ($\omega_v = 0.7$) 0.166908 ($\omega_v = 1.5$)
$GJ/m\Omega^2R^4$	0.000925 ($\omega_\phi = 2.5$) 0.005661 ($\omega_\phi = 5$)
k_{m_1}/R	0
k_{m_2}/R	0.025
k_A/k_m	1.5
c/R	$\pi/40$
β_p	0.05 rad
σ	0.1
γ	5
a	6
c_0	0
c_1	6
d_0	0.0095
d_1	0
d_2	0
$C_{M_{ss}}$	0
k_h	1.15

Table 2. Steady tip deflections of a hingeless rotor blade

Number of elements	$v_{0_{tip}}/R$	$w_{0_{tip}}/R$	$\hat{\phi}_{0_{tip}}$
2	-0.00350	0.00487	-0.04386
3	-0.00342	0.00459	-0.04334
4	-0.00338	0.00446	-0.04315
5	-0.00337	0.00440	-0.04307
6	-0.00336	0.00436	-0.04302
7	-0.00335	0.00434	-0.04299
8	-0.00335	0.00433	-0.04297

($C_T/\sigma = 0.1$, $\beta_p = 0.05\,rad$, $\gamma = 5.0$, $\omega_v = 1.5\Omega$, $\omega_w = 1.15\Omega$, $\omega_\phi = 2.5\Omega$)

Table 2. Fundamental Coupled natural frequencies of a hingeless rotor blade

Number of elements	ω_v/Ω	ω_w/Ω	ω_ϕ/Ω
2	1.5196	1.1251	2.5105
3	1.5184	1.1221	2.4872
4	1.5182	1.1214	2.4787
5	1.5181	1.1212	2.4746
6	1.5181	1.1211	2.4724
7	1.5181	1.1211	2.4710
8	1.5180	1.1210	2.4702

($C_T/\sigma = 0.1$, $\beta_p = 0.05\,rad$, $\gamma = 5.0$, $\omega_v = 1.5\Omega$, $\omega_w = 1.15\Omega$, $\omega_\phi = 2.5\Omega$)

Table 4. Real parts of the flutter eigenvalues of a hingeless rotor blade

Number of modes	Lead-lag	Flap	Torsion
3	-0.03074	-0.31488	-0.35148
4	-0.03049	-0.31383	-0.35049
5	-0.03034	-0.31443	-0.35207
6	-0.03034	-0.31442	-0.35206
7	-0.03034	-0.31448	-0.35209

($C_T/\sigma = 0.1$, $\beta_p = 0.05\,rad$, $\gamma = 5.0$, $\omega_\psi = 1.5\Omega$, $\omega_w = 1.15\Omega$, $\omega_\phi = 2.5\Omega$)

Table 5. Steady tip deflections of an articulated rotor blade

Number of elements	$v_{0_{tip}}/R$	$w_{0_{tip}}/R$	$\hat{\phi}_{0_{tip}}$
2	-0.06040	0.01274	-0.04476
3	-0.06001	0.01238	-0.04425
4	-0.05987	0.01224	-0.04405
5	-0.05980	0.01217	-0.04396
6	-0.05977	0.01212	-0.04391
7	-0.05975	0.01210	-0.04388
8	-0.05973	0.01208	-0.04386

($C_T/\sigma = 0.1$, $\beta_p = 0.05\,rad$, $\gamma = 5.0$, Hinge offset $= 0.06R$, $\omega_\phi = 2.5\Omega$)

Table 6. Fundamental Coupled natural frequencies of an articulated rotor blade

Number of elements	ω_v/Ω	ω_w/Ω	ω_ϕ/Ω
2	0.2999	1.0440	2.5285
3	0.2999	1.0440	2.5049
4	0.2999	1.0440	2.4963
5	0.2999	1.0440	2.4923
6	0.2999	1.0440	2.4901
7	0.2999	1.0440	2.4889
8	0.2999	1.0440	2.4878

($C_T/\sigma \approx 0.1$, $\beta_p = 0.05\,rad$, $\gamma = 5.0$, Hinge offset $= 0.06R$, $\omega_\phi = 2.5\Omega$)

Table 7. Real parts of the flutter eigenvalues of an articulated rotor blade

Number of modes	Lead-lag	Flap	Torsion
3	-0.00955	-0.33926	-0.39160
4	-0.00951	-0.34108	-0.39338
5	-0.00957	-0.34498	-0.39471
6	-0.00953	-0.34232	-0.39448
7	-0.00953	-0.34230	-0.39449

($C_T/\sigma = 0.1$, $\beta_p = 0.05\,rad$, $\gamma = 5.0$, Hinge offset $= 0.06R$, $\omega_\phi = 2.5\Omega$)

Table 8. Structural properties of a bearingless blade

Property	Outboard blade	Each flexbeam	Torque tube
$EI_y/m_0\Omega^2R^4$	0.026655 0.014486	0.013328 0.007243	0.001 0.001
$EI_z/m_0\Omega^2R^4$	0.166908	0.083454	0.001
$GJ/m_0\Omega^2R^4$	0.000925 0.005661	0.000463 0.002830	0.02 0.02
k_{m_1}/R	0	0	0
k_{m_2}/R	0.025	0.025	0.01
k_A/k_m	1.5	1.5	1
m/m_0	1	0.5	0.1

Table 9. Steady tip deflections of a twinbeam model
(Zero inboard pitch)

Number of elements						
Flexbeam one	Flexbeam two	Outboard blade	$u_{0_{tip}}/R$	$v_{0_{tip}}/R$	$w_{0_{tip}}/R$	$\hat{\phi}_{0_{tip}}$
1	1	2	0.001613	-0.003750	0.011214	-0.030734
2	2	1	0.001614	-0.003794	0.011289	-0.030634
2	2	2	0.001613	-0.003750	0.011213	-0.030735
2	2	3	0.001613	-0.003747	0.011206	-0.030732
3	3	2	0.001613	-0.003750	0.011213	-0.030735

($C_T/\sigma = 0.1$, $\beta_p = 0.05\,rad$, $\gamma = 5.0$, $\omega_v = 1.87\Omega$, $\omega_w = 1.15\Omega$, $\omega_\phi = 2.91\Omega$)

Table 10. Fundamental natural frequencies of a twinbeam model
(Zero inboard pitch)

Number of elements					
Flexbeam one	Flexbeam two	Outboard blade	ω_v/Ω	ω_w/Ω	ω_ϕ/Ω
1	1	2	1.77973	1.15018	2.88149
2	2	1	1.78825	1.15027	2.89491
2	2	2	1.77962	1.14977	2.88144
2	2	3	1.77877	1.14971	2.88094
3	3	2	1.77961	1.14974	2.88141

($C_T/\sigma = 0.1$, $\beta_p = 0.05\,rad$, $\gamma = 5.0$, $\omega_v = 1.87\Omega$, $\omega_w = 1.15\Omega$, $\omega_\phi = 2.91\Omega$)

Table 11. Real parts of the flutter eigenvalues of a twinbeam model
(Zero inboard pitch)

Number of modes	Lead-lag	Flap	Torsion
3	0.00506	-0.35029	-0.38113
4	0.00450	-0.35228	-0.38094
5	0.00445	-0.35267	-0.38119
6	0.00445	-0.35267	-0.38119

($C_T/\sigma = 0.1$, $\beta_p = 0.05\,rad$, $\gamma = 5.0$, $\omega_\nu = 1.87\Omega$, $\omega_w = 1.15\Omega$, $\omega_\phi = 2.91\Omega$)

Table 12. Fundamental natural frequencies at various thrust levels
(Zero inboard pitch)

C_T/σ	Lead-lag		Flap		Torsion	
	Twin	Eqvlt.	Twin	Eqvlt.	Twin	Eqvlt.
0	1.870	1.866	1.149	1.149	2.910	2.910
0.04	1.864	1.886	1.152	1.142	2.921	2.900
0.08	1.851	1.896	1.157	1.129	2.930	2.887
0.12	1.830	1.894	1.161	1.112	2.934	2.875
0.16	1.805	1.878	1.163	1.091	2.930	2.864
0.2	1.775	1.849	1.162	1.066	2.916	2.854

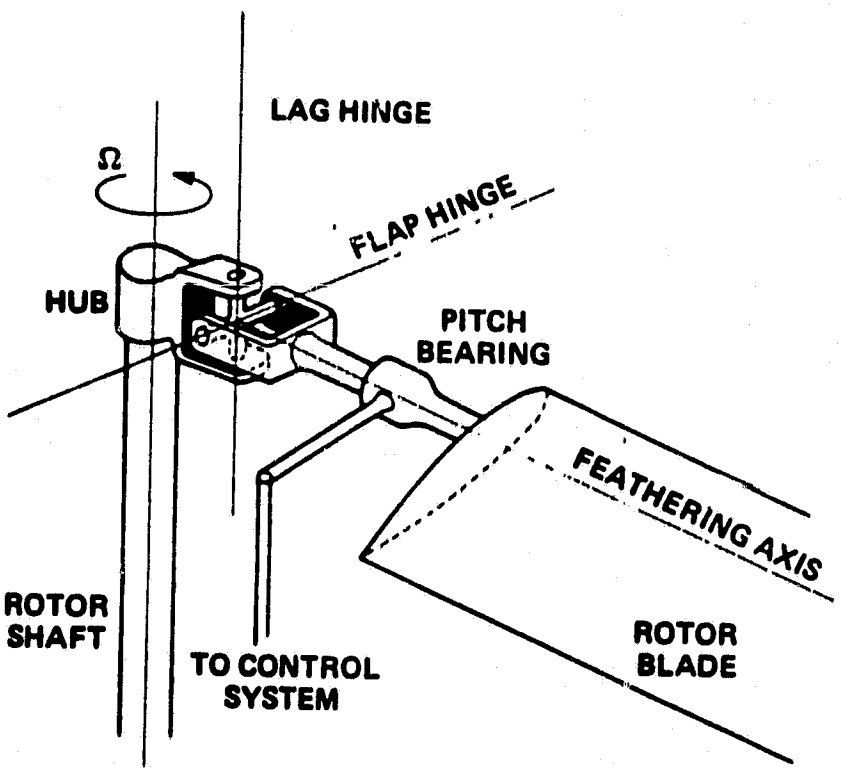

Fig. 1 Schematic of an articulated rotor hub and root.

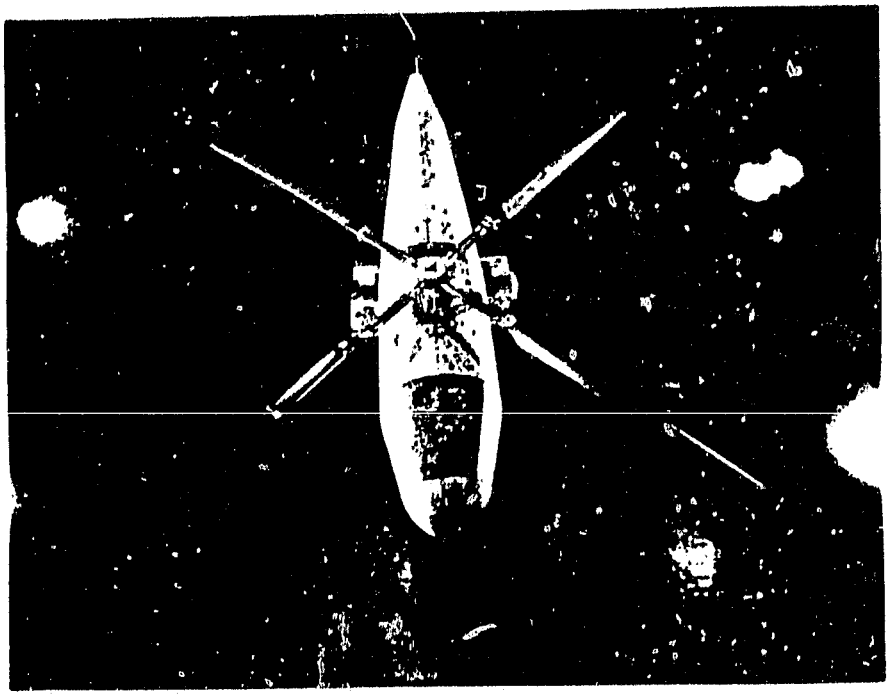

Fig. 2 Bearingless Main Rotor (BMR)

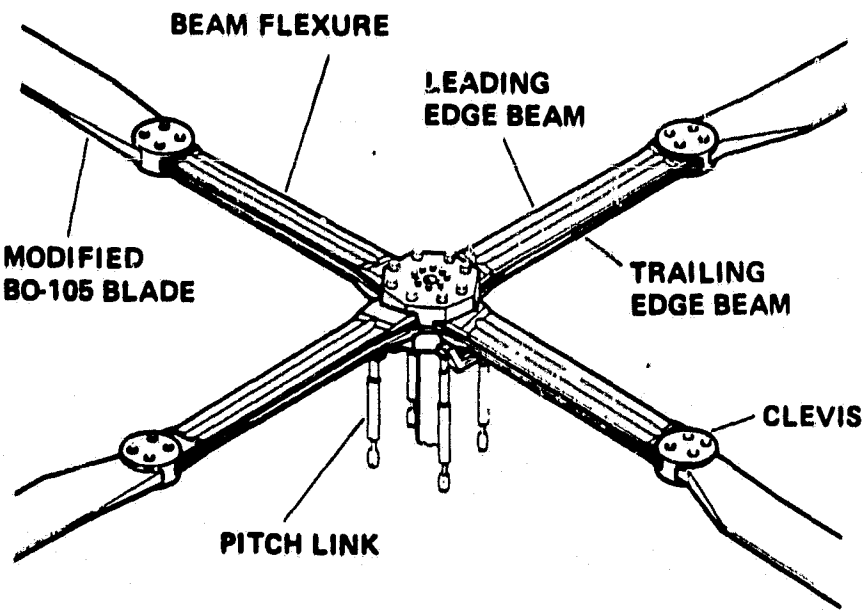

Fig. 3 Flexure of BMR

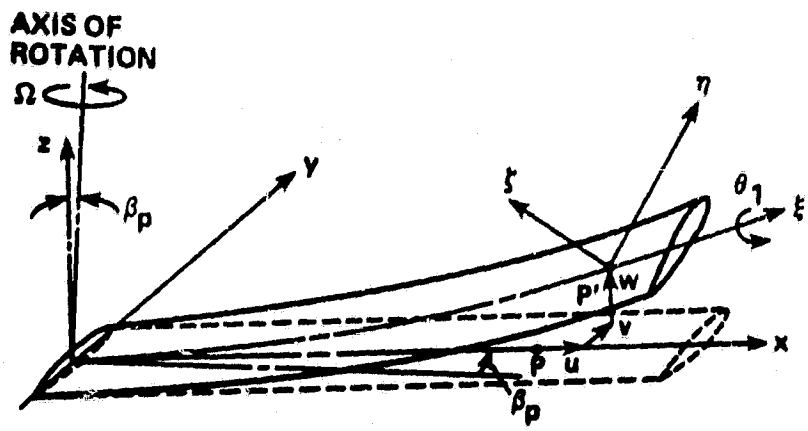

Fig. 4 Blade coordinate systems and deflections

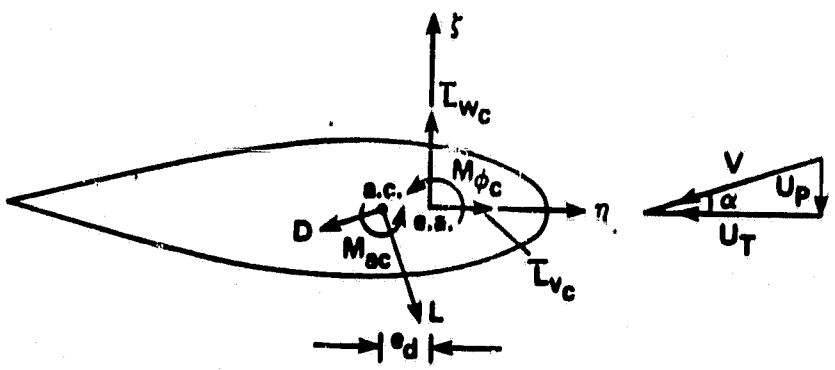

Fig. 5 Deformed-blade-section aerodnamics

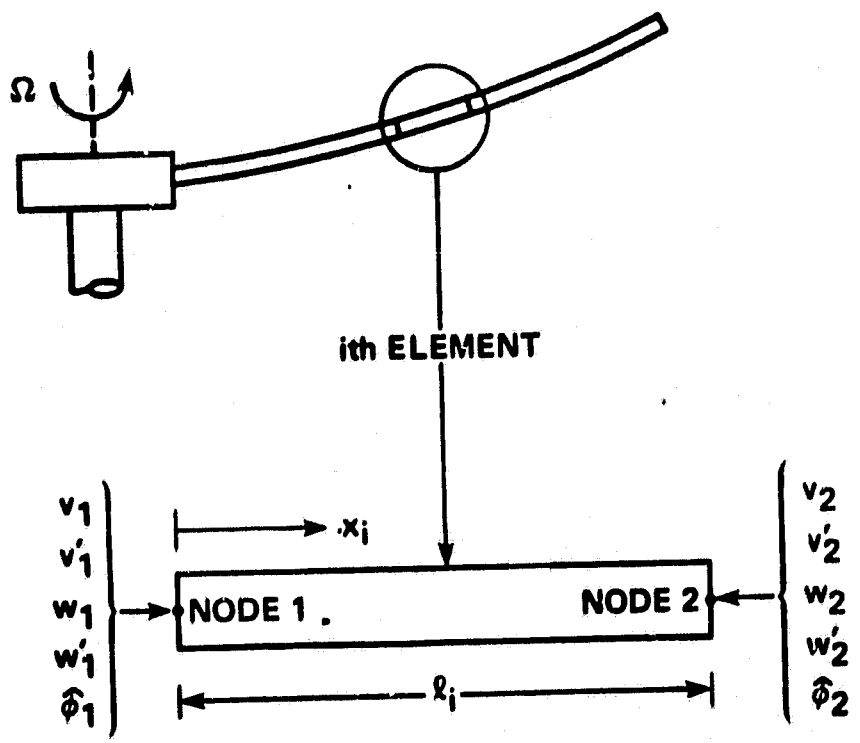

Fig. 6 A finite element showing nodal degrees of freedom

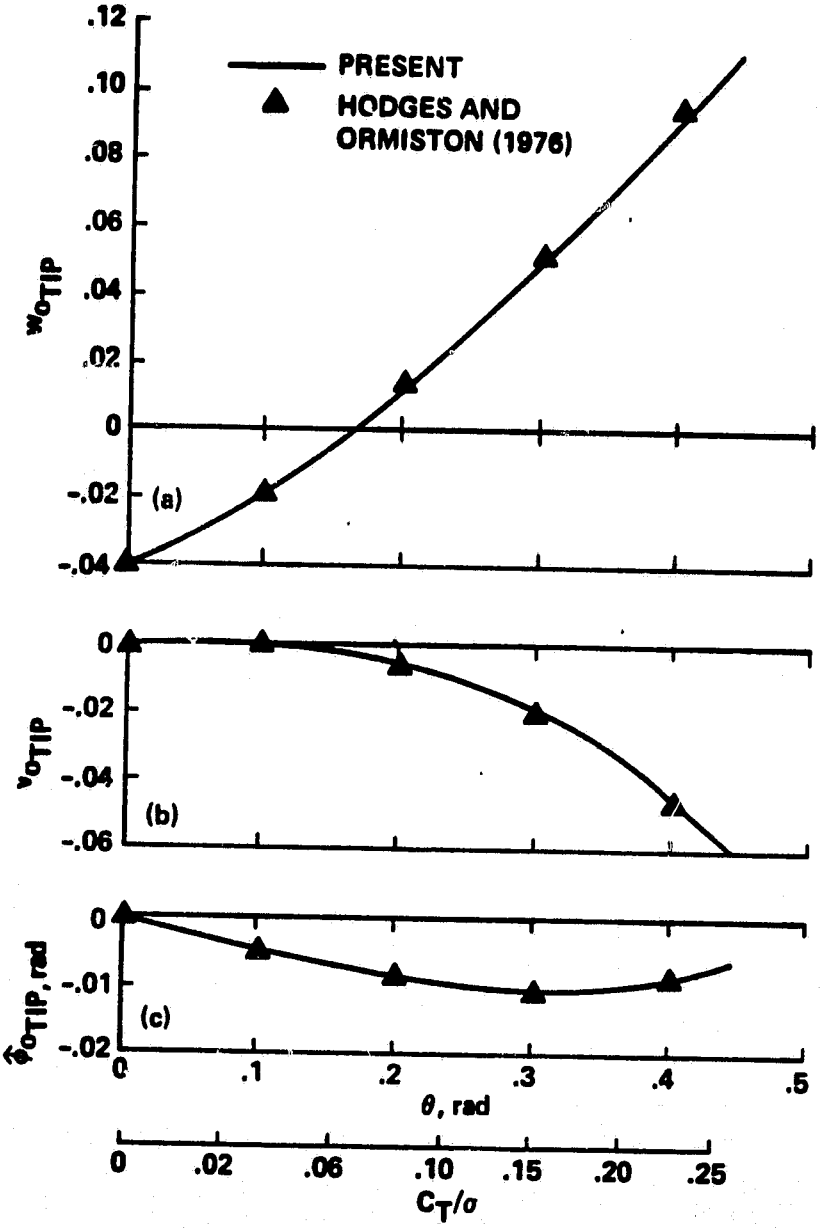

Fig. 7 (a) Flap bending (b) lead-lag bending (c) torsion. Steady tip deflections of a stiff-inplane hingeless rotor blade; $\omega_v = 1.5\Omega$, $\omega_w = 1.15\Omega$, $\omega_\phi = 5.0\Omega$, $\gamma = 5.0$, $\beta_p = 0.05\,rad$.

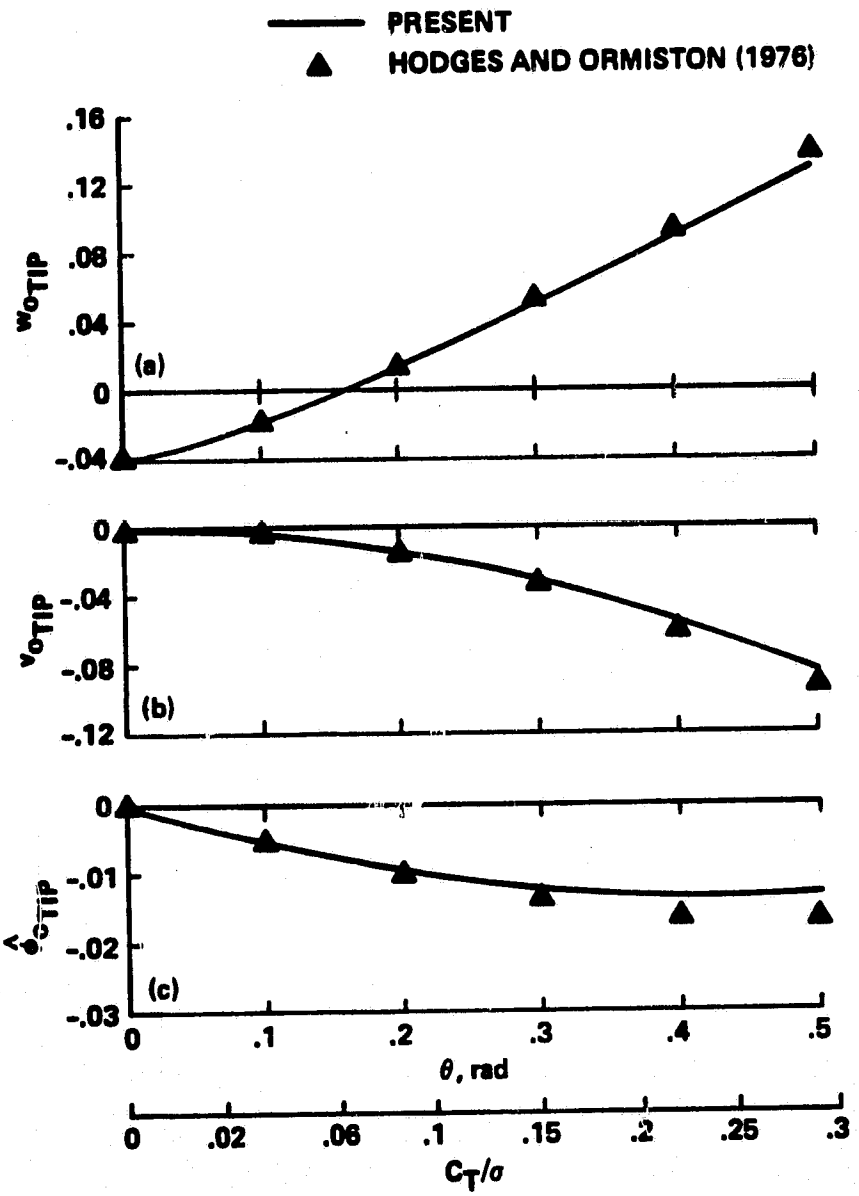

Fig. 8 (a) Flap bending (b) lead-lag bending (c) torsion. Steady tip deflections of a soft-inplane hingeless rotor blade; $\omega_v = 0.7\Omega$, $\omega_w = 1.15\Omega$, $\omega_\phi = 5.0\Omega$, $\gamma = 5.0$, $\beta_p = 0.05\,rad$.

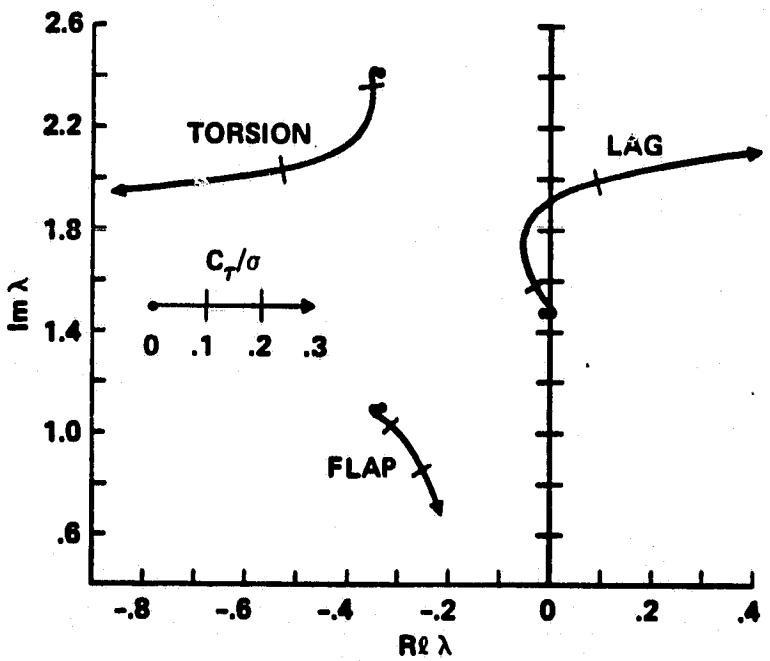

Fig. 9 Root locus plot for a hingeless rotor blade; $\omega_v = 1.5\Omega$, $\omega_w = 1.15\Omega$, $\omega_\phi = 2.5\Omega$, $\gamma = 5.0$, $\beta_p = 0.05\,rad.$

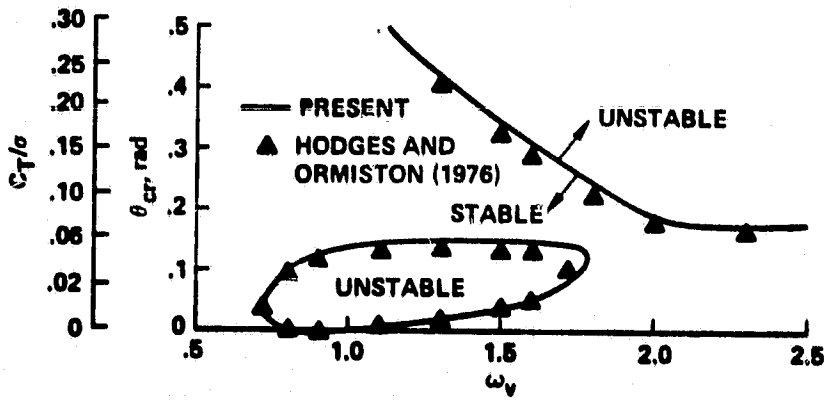

Fig. 10 Stability boundaries for a hingeless rotor blade; $\omega_\omega = 1.15\Omega$, $\omega_\phi = 2.5\Omega$, $\gamma = 5.0$, $\beta_p = 0.05\,rad$.

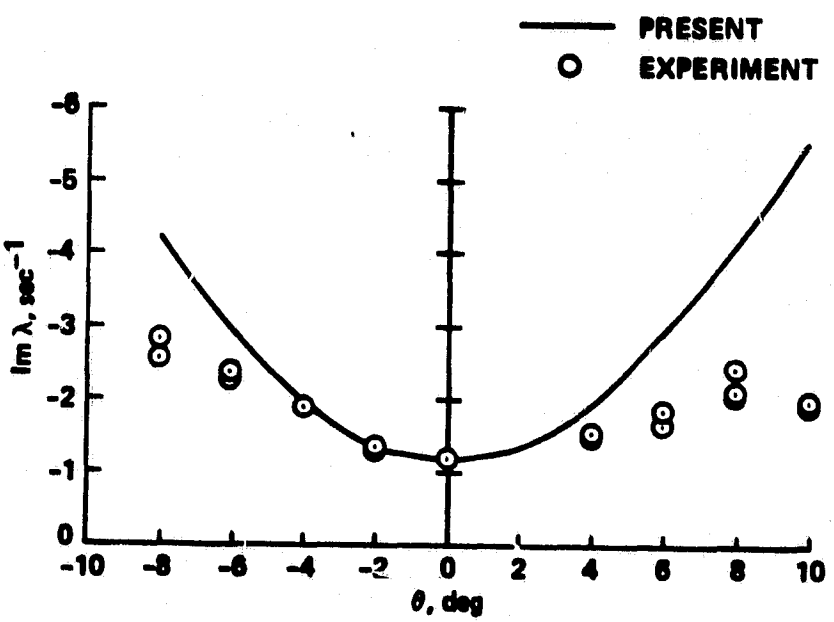

Fig. 11 Comparison of hingelesss rotor blade results with experimental results.

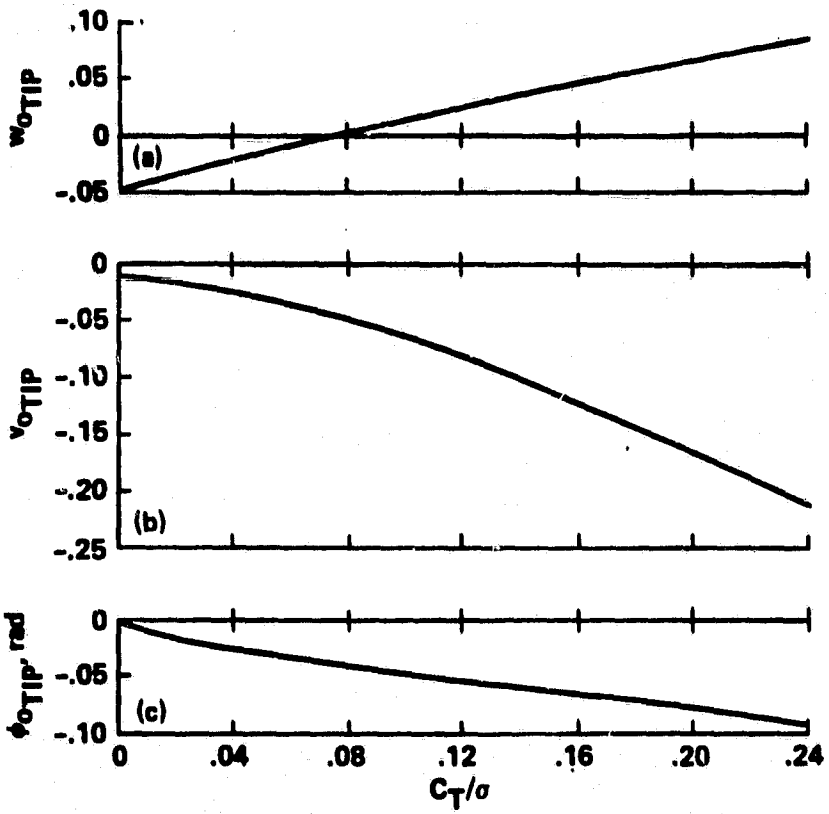

Fig. 12 a) Flap bending, b) lead-lag bending c) torsion. Steady tip deflections of an articulated rotor blade; hinge offset=0.06R, $\omega_\phi = 2.5\Omega$, $\gamma = 5.0$, $\beta_p = 0.05\,rad.$

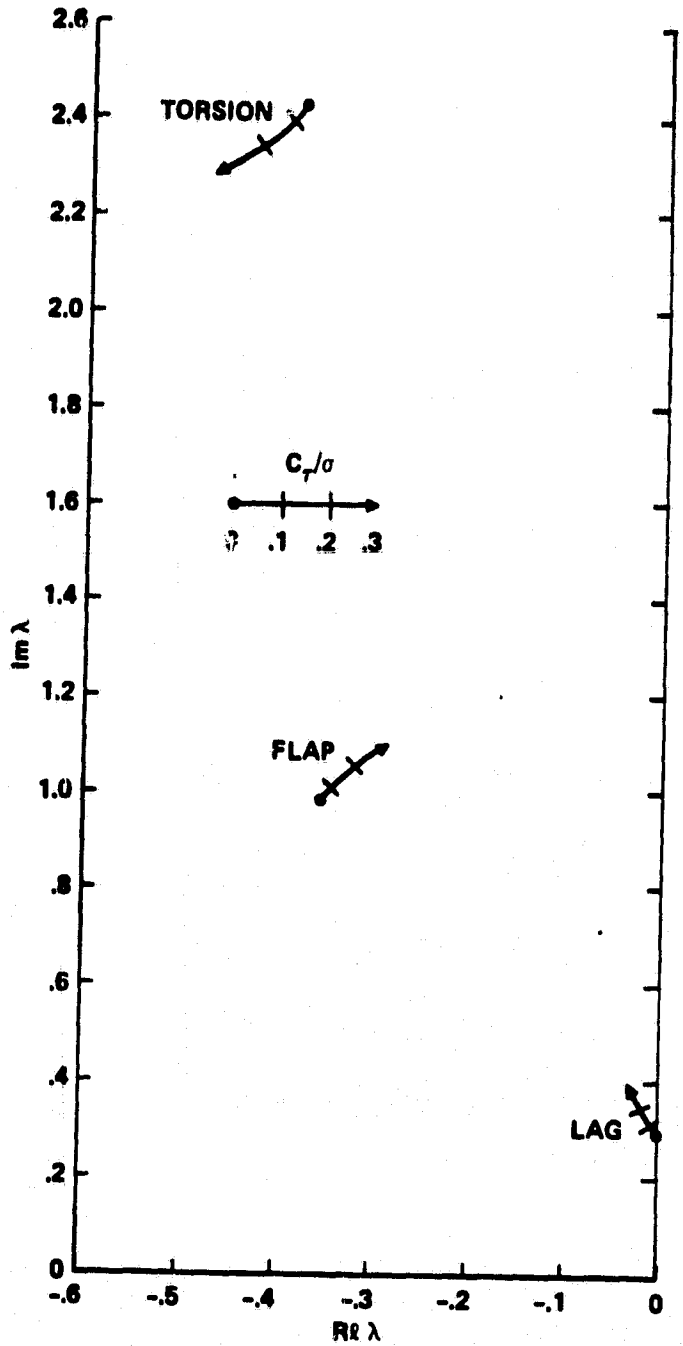

Fig. 13 Root locus plot for an articulated rotor blade; hinge offset=0.06R, $\omega_\phi = 2.5\Omega$, $\gamma = 5.0$, $\beta_p = 0.05\,rad.$

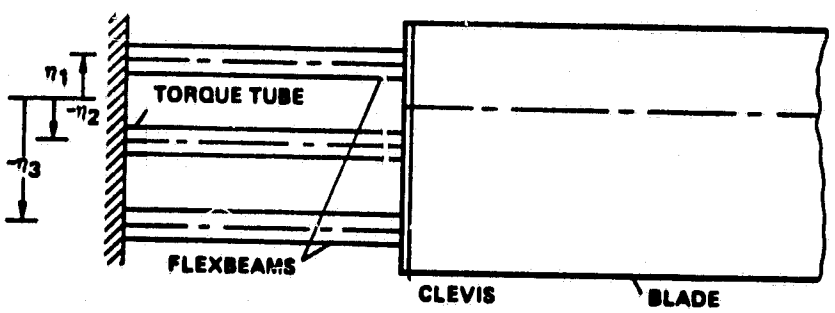

Fig. 14 Analytical model of a bearingless blade.

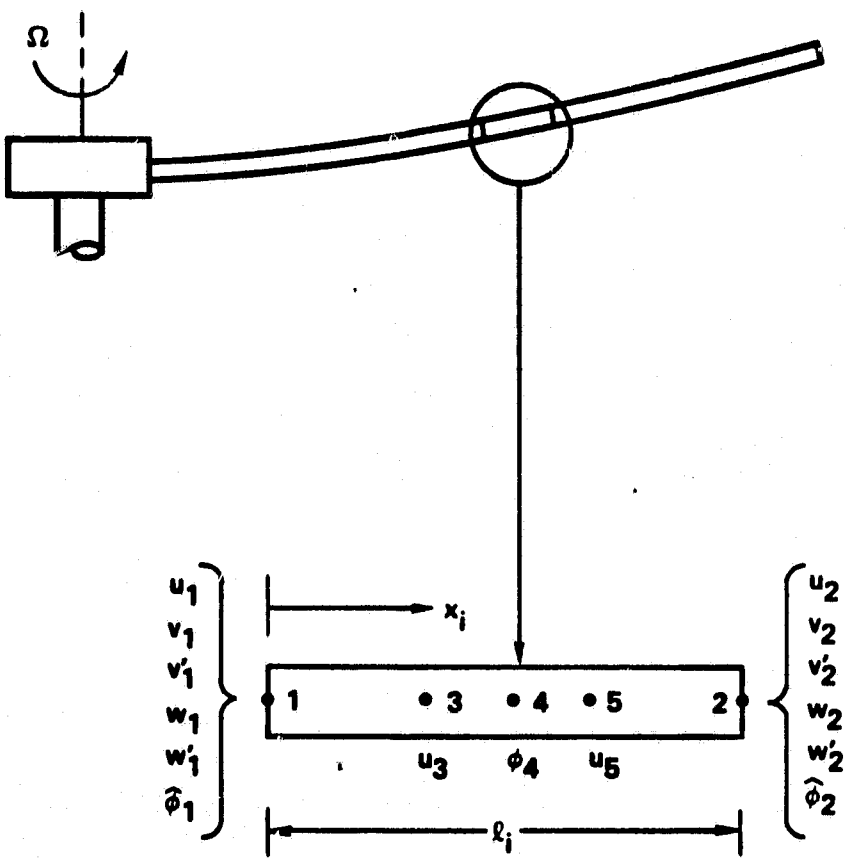

Fig. 15 Refined finite element for multiple-load-path blades.

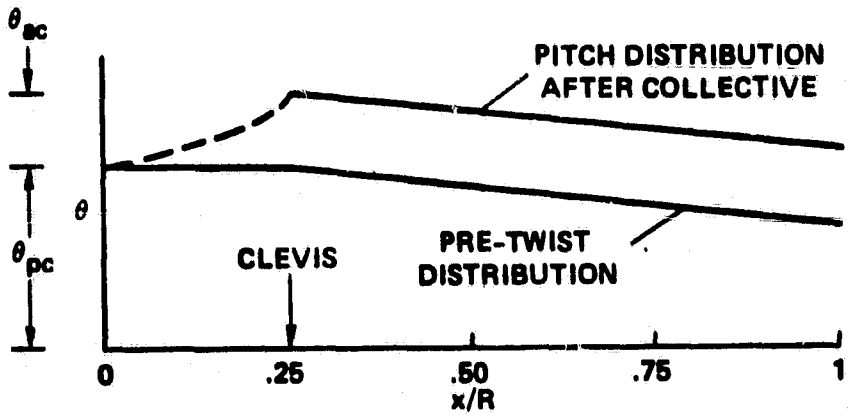

Fig. 16 Pitch distribution of a bearingless rotor blade.

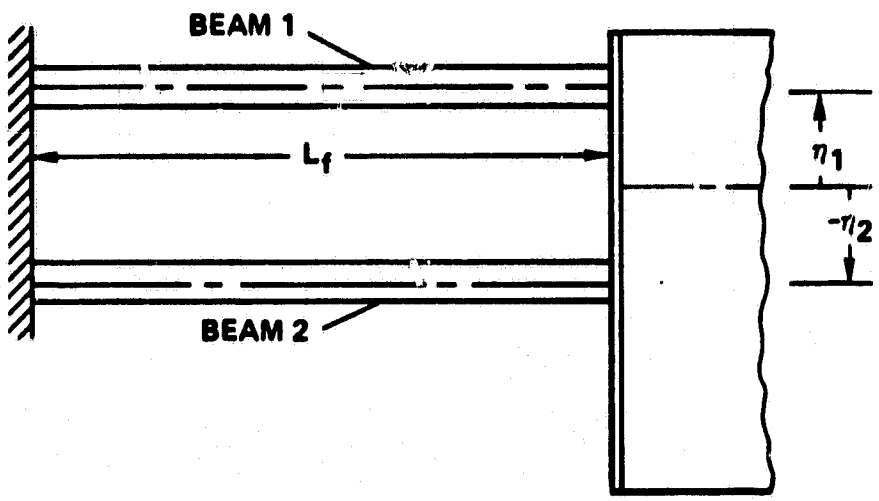

Fig. 17 Twinbeam multiple-load-path blade model.

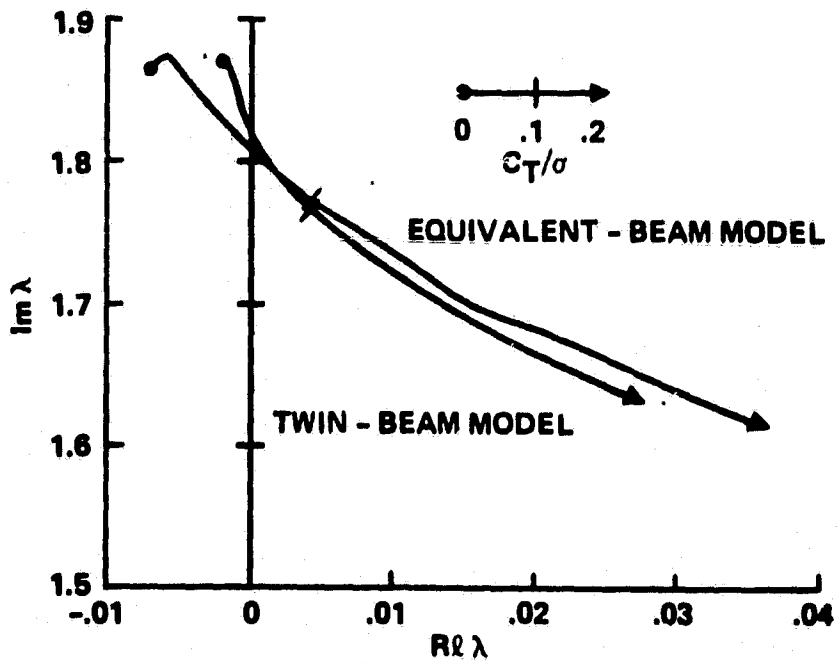

Fig. 18 Root locus plot of lead-lag mode of stiff-inplane, soft-in-torsion twinbeam model (zero inboard pitch); $\omega_v = 1.87\Omega$, $\omega_w = 1.15\Omega$, $\omega_\phi = 2.91\Omega$, $\gamma = 5.0$, $\beta_p = 0.05\,rad.$

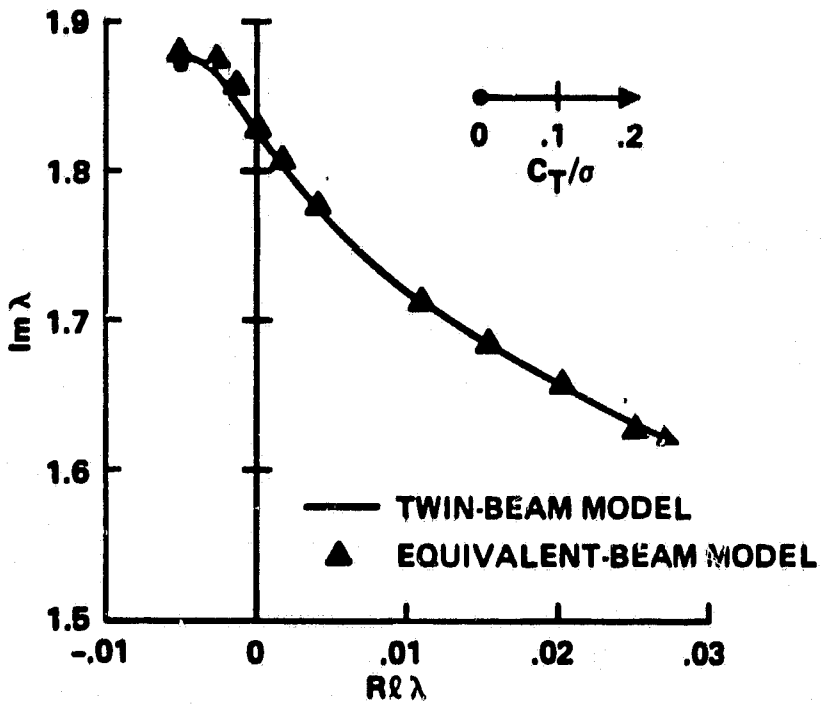

Fig. 10 Root locus plot of lead-lag mode of stiff-inplane, soft-in-torsion twinbeam model (zero inboard pitch; coupling structural stiffness terms of nonlinear origin suppressed in flutter analysis); $\omega_v = 1.87\Omega$, $\omega_w = 1.15\Omega$, $\omega_\phi = 2.91\Omega$, $\gamma = 5.0$, $\beta_p = 0.05$ *rad*.

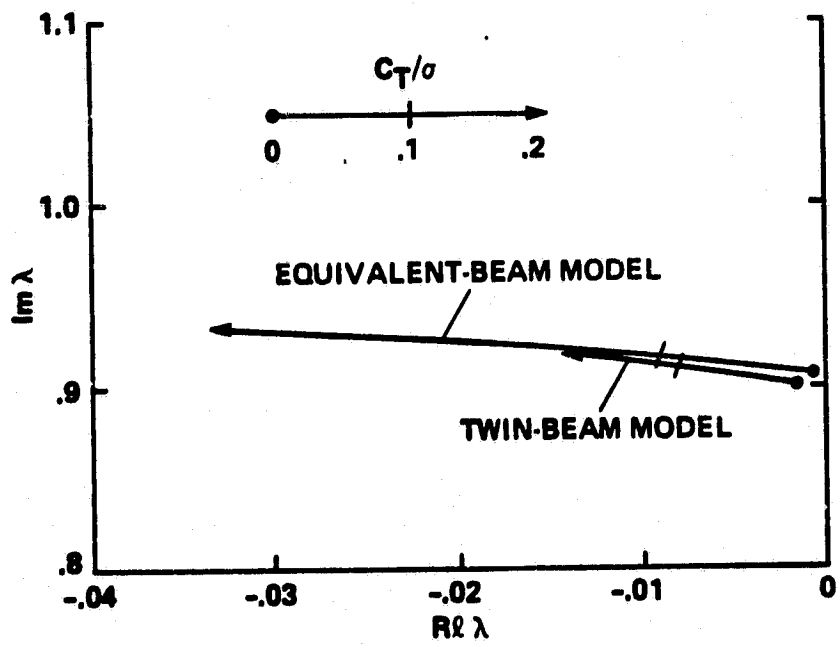

Fig. 20 Root locus plot of lead-lag mode of soft-inplane, soft-in-torsion twinbeam model (zero inboard pitch); $\omega_v = 0.90\Omega$, $\omega_w = 1.15\Omega$, $\omega_\phi = 2.91\Omega$, $\gamma = 5.0$, $\beta_p = 0.05\,rad.$

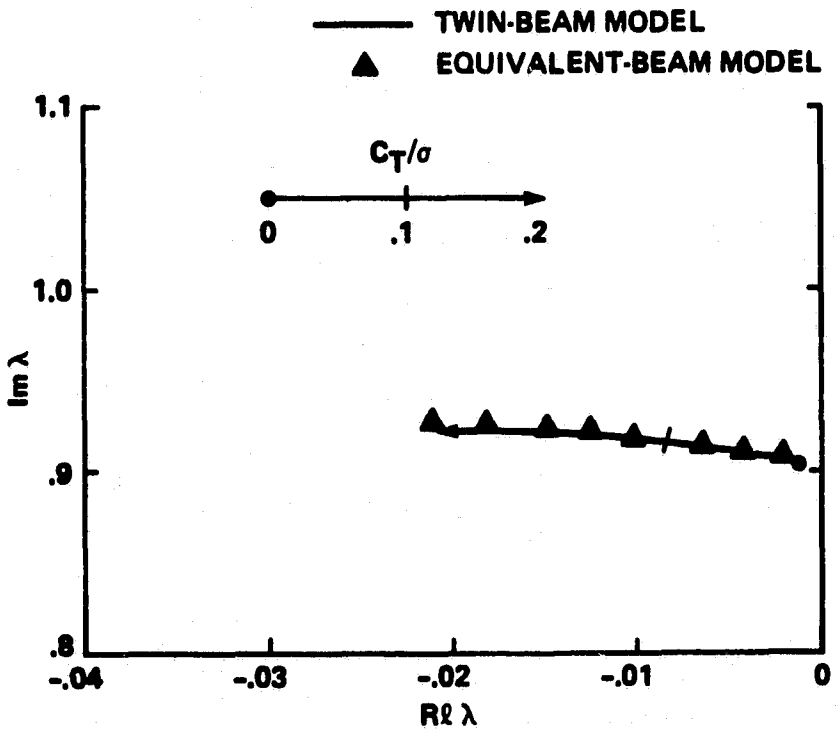

Fig. 21 Root locus plot of lead-lag mode of soft-inplane, soft-in-torsion twinbeam model (zero inboard pitch; coupling structural stiffness terms of nonlinear origin suppressed in flutter analysis); $\omega_v = 0.90\Omega$, $\omega_w = 1.15\Omega$, $\omega_\phi = 2.91\Omega$, $\gamma = 5.0$, $\beta_p = 0.05\,rad.$

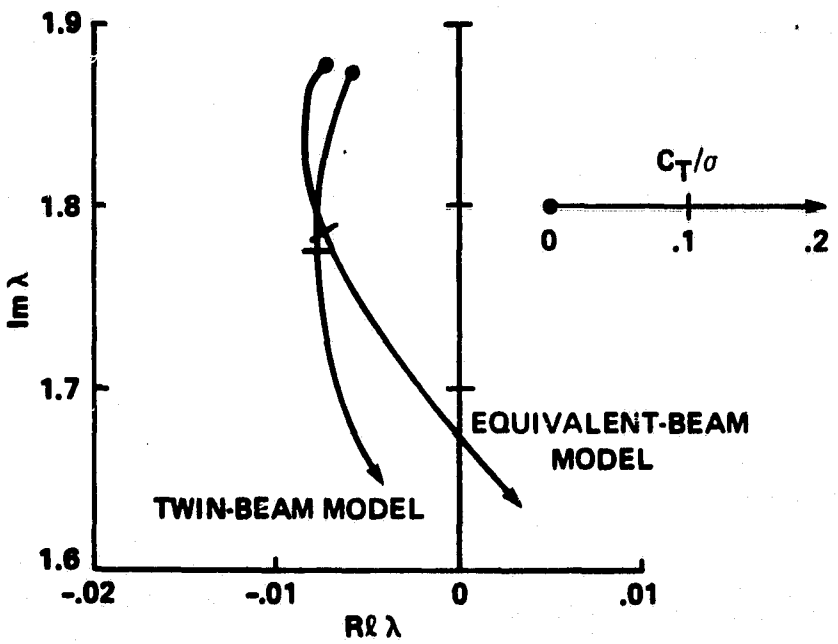

Fig. 22 Root locus plot of lead-lag mode of stiff-inplane, stiff-in-torsion twinbeam model (zero inboard pitch); $\omega_v = 1.87\Omega$, $\omega_w = 1.15\Omega$, $\omega_\phi = 5.38\Omega$, $\gamma = 5.0$, $\beta_p = 0.05\,rad.$

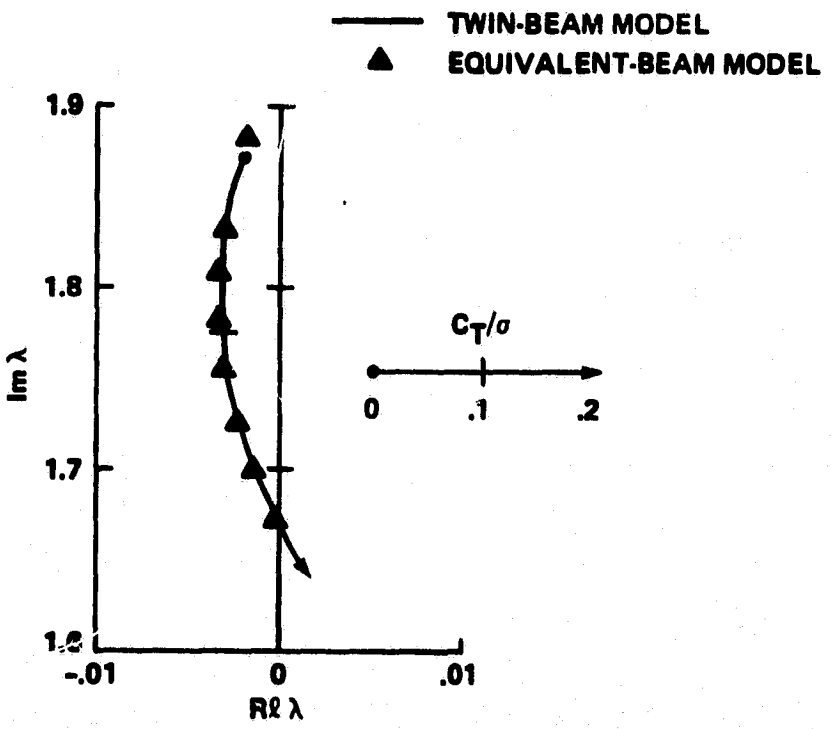

Fig. 23 Root locus plot of lead-lag mode of stiff-inplane, stiff-in-torsion twinbeam model (zero inboard pitch); coupling structural stiffness terms of nonlinear origin suppressed in flutter analysis); $\omega_v = 1.87\Omega$, $\omega_w = 1.15\Omega$, $\omega_\phi = 5.38\Omega$, $\gamma = 5.0$, $\beta_p = 0.05\,rad.$

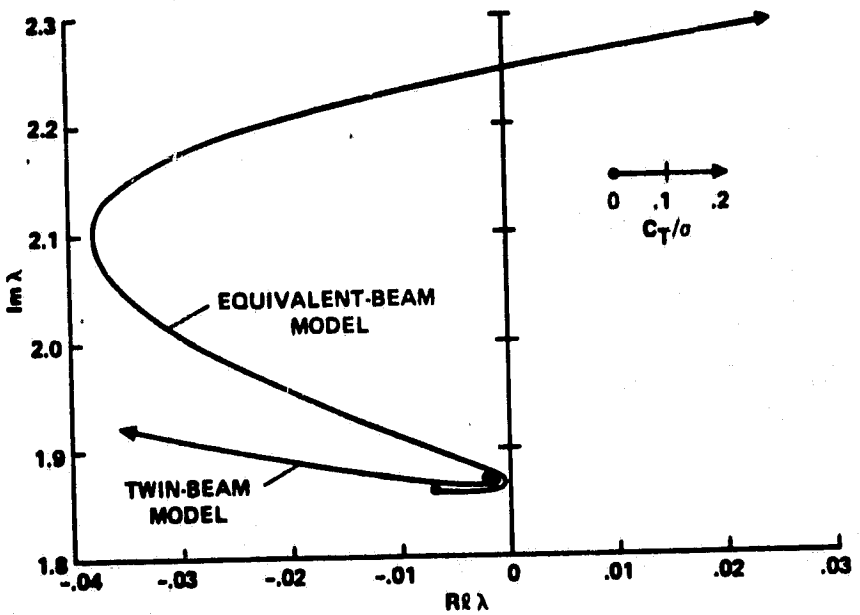

Fig. 24 Root locus plot of lead-lag mode of stiff-inplane, soft-in-torsion twinbeam model (same pitch for inboard and outboard); $\omega_v = 1.87\Omega$, $\omega_w = 1.15\Omega$, $\omega_\phi = 2.91\Omega$, $\gamma = 5.0$, $\beta_p = 0.05\,rad$.

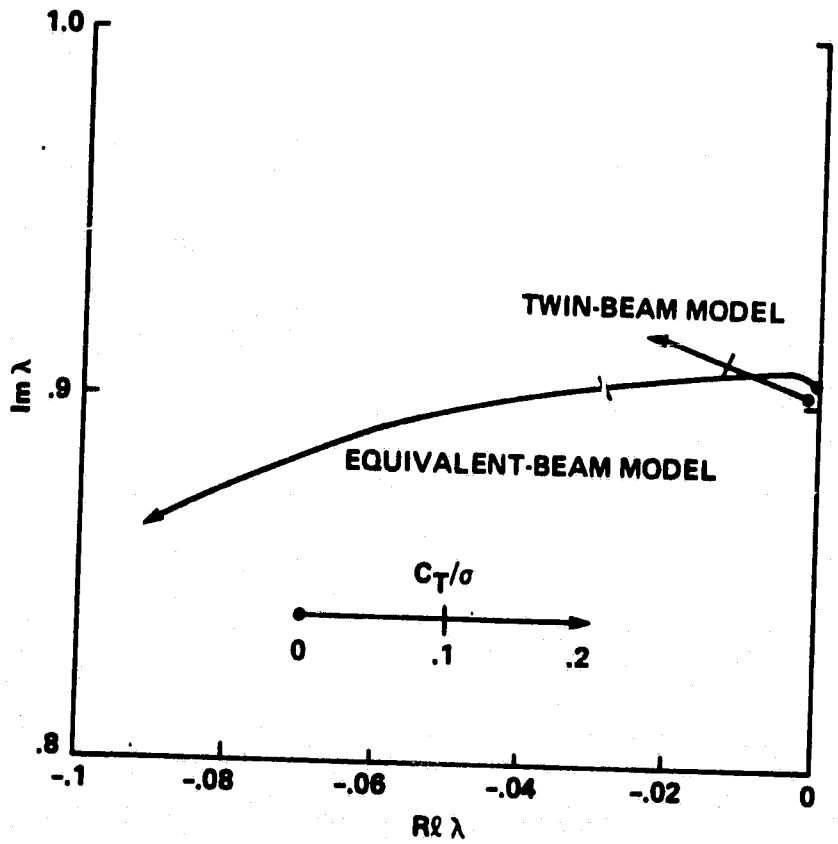

Fig. 25 Root locus plot of lead-lag mode of soft-inplane, soft-in-torsion twinbeam model (same pitch for inboard and outboard); $\omega_v = 0.90\Omega$, $\omega_w = 1.15\Omega$, $\omega_\phi = 2.91\Omega$, $\gamma = 5.0$, $\beta_p = 0.05\,rad.$

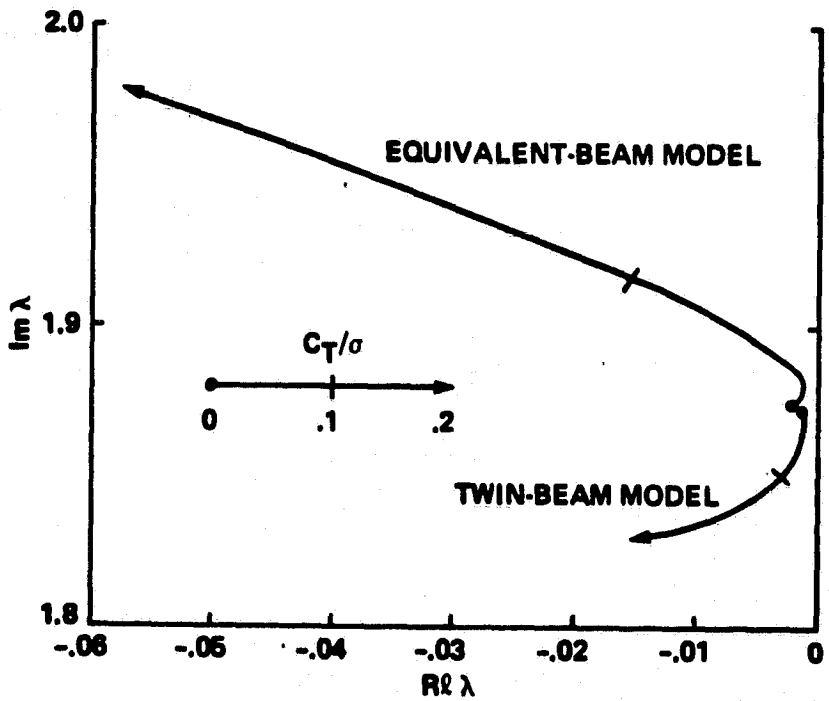

Fig. 26 Root locus plot of lead-lag mode of stiff-inplane, stiff-in-torsion twinbeam model (same pitch for inboard and outboard); $\omega_v = 1.87\Omega$, $\omega_w = 1.15\Omega$, $\omega_\phi = 5.38\Omega$, $\gamma = 5.0$, $\beta_p = 0.05\,rad.$

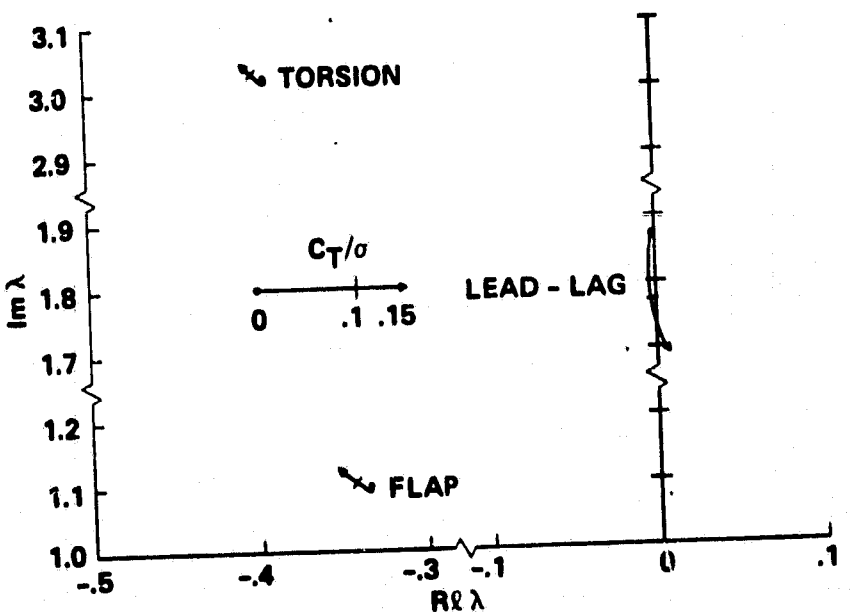

Fig. 27 Root locus plot of a bearingless blade with two identical flexbeams and a torque tube; $\omega_v = 1.87\Omega$, $\omega_w = 1.15\Omega$, $\omega_\phi = 3.10\Omega$, $\gamma = 5.0$, $\beta_p = 0.05\,rad.$